PRESSURE DROP IN HIGH DENSITY POROUS METAL VIA TOMOGRAPHY DATASETS

BY

MUHAMMAD, Mahmud Salihu

M.Eng/SEET/2017/6761

DEPARTMENT OF CHEMICAL ENGINEERING

FEDERAL UNIVERSITY OF TECHNOLOGY MINNA

OCTOBER, 2021.

PRESSURE DROP IN HIGH DENSITY POROUS METAL VIA TOMOGRAPHY DATASETS

BY

MUHAMMAD, Mahmud Salihu

M.Eng/SEET/2017/6761

A THESIS SUBMITTED TO THE POSTGRADUATE SCHOOL FEDERAL UNIVERSITY OF TECHNOLOGY, MINNA, NIGERIA. IN PARTIAL FULFILLMENT OF THE REQUIREMENTS FOR THE AWARD OF THE DEGREE OF MASTER OF ENGINEERING (M.Eng) IN CHEMICAL ENGINEERING.

OCTOBER, 2021.

ABSTRACT

There is little or no published articles on Computational Fluid Dynamics (CFD) approach to study the contributory effect of sudden change in pore- volume on the flow behaviour of high density porous structures using CFD approach coupled with 3D advanced imaging techniques. This study combines three-dimensional advanced imaging techniques and computational fluid dynamic modelling and simulation (CFD) to characterise the pressure drop of flowing fluid across high-density porous metals utilising high-resolution X-ray computed tomography datasets. The modelling approach quantifies the combined effects of pore volume fraction (80 to 95%), pore connectivity, pore size (0.2 to 5.0 mm) and morphology on the flow behaviour of porous metals and to study in more detail the pressure drop behaviour characterised by the sudden change in pore volume by stacking of differential porous samples at the pore-level. Numerically, the pressure drop at velocity $1 m.s^{-1}$ of Inc 450µm and Inc 12000µm are 112.48 pa and 14.52 pa respectively and after stacking the both samples the pressure drop at same velocity is 72.57 pa. The resulting predicted values of the pressure drop as a function of superficial fluid velocity ranging from Darcy to Turbulent fluid flow regimes were used to account for the permeability (k_0) and Form drag coefficient (C) of these materials. From literature the measured values of permeability and Form drag coefficient for the 20mm thick Inc 450µm sample are $1.69 \pm 0.03 \times 10^{-09}$ m^2 and 8566.4 ± 150 m^{-1} respectively while the CFD computed values of the permeability and Form drag coefficient for this range of superficial fluid velocities are 1.60×10^{-09} m^2 and $8530.8 m^{-1}$ respectively. Supportable agreement between CFD modelled data against empirical measurements available in the literature was substantiated. Therefore it is considered that this approach could lead practically to minimizing the number of design iterations required for the processing of novel-attributing porous metallic materials for applications involving fluid flow.

TABLE OF CONTENTS

LIST OF TABLES

LIST OF FIGURES

NOMENCLATURE

CFD Computational Fluid Dynamics α

Viscous

μ Dynamic Viscosity

K_o Permeability

C Form drag coefficient

C_F Forchheimer Coefficient

V_p Pore Velocity

V_s Superficial Fluid Velocity C_T

Computed Tomography D_p Pore

Diameter

D_W Pore Connectivity

L_G Ligament thickness

$\int$ Fluid density

ε Porosity

BC Boundary Condition

$\sigma_{FB.}$ Ratio of the structure surface area to bulk volume

σ_{FF} Ratio of the structure surface area to structure volume Inc.

Inconel™ (Alantum™)

RCM-NCX Recemat™

PPI Pore per Inch

CHAPTER ONE

1.0 INTRODUCTION

1.1 Background of Study

In recent year, studies involving fluid flow through porous material especially those from metals and metal alloys have attracted a wider range of attention in various field of science, engineering, environmental and industrial application. These include filters for high-temperature gas and fluid filtration, oil and gas, biomedical devices, thermal exchanger in heat exchanger, aero-engine fluid systems, and catalytic-reactor for conversion of toxic gases, load bearing and vibrational control devices. Porous metal are suitable for these applications due to its essential properties like; high surface area, effective thermal conductivity, low density, high stiffness, good energy/sound absorption and high heat resistance (Zhong *et al.*, 2014; Della Torre *et al.*, 2014; Oun and Kennedy, 2014; De Carvalho *et al.*, 2017; Ahmed *et al.*, 2018; Otaru *et al*., 2019).

Analogous research work on effects in solving problem concerning porous metals was attempted, but accurate modeling behaviour of pressure drop/gradient is a major concern. A survey from literature stated that studying and then controlling pressure drop across porous metals is an important factor for optimising the function of these structures and to create a new structure with improved properties (Kennedy, 2012; Dukhan, 2013; Ranut *et al.*, 2014; Otaru *et al*., 2018a).

Analogous research work reported that pressure drop developed across these structures depends mainly both on the fluid properties and on the permeability of porous metal, which is influenced by the porosity, cell size and morphology of the pores and pore network (Choe, 2004; Dukhan, 2006; Oun and Kennedy, 2014). Baloyo (2016) also reported that

passage of fluid freely through porous material is a simple definition of permeability. In addition, permeability is dependent on the structural nature of material, that is, porosity and packing arrangements.

Applicable theories exist between porous metallic structures and packed beds (Despois and Mortensen, (2005); Oun and Kennedy, (2014); Kouidri and Madani, (2016); Otaru, (2019)). Fluid flow with very slow velocity, characterised by pore diameter Reynolds number (N_{Re}) lees than one (N_{Re} <1), the acknowledged Darcy's law relates the fluid velocity and unit pressure drop developed across porous structures. Fluid flow with high velocity, the Darcy-Dupuit-Forchheimer model relates the defined pressure drop per unit flow thickness developed across porous materials as a function of the two most important parameters used to describe flow behaviour at very low permeability (k_o) and high Form drag coefficient (C). Despois and Mortensen (2005); Kouidri and Madani (2016); Otaru *et al*., (2018b); Otaru (2019) performed an experimental study on pressure gradient across porous metallic structure using Darcy-Dupuit-Forchheimer expression to determine the permeability and form drag coefficient of flowing fluid through these structure and also been proved for good understanding and quantifying the effect of pore related parameters and structural nature of fluid flow across porous metals. Despite the numerous flows applicability of microcellular structures there is little or no evidently related published article on sudden changes associated with pore volume of these materials when subjected to the penetration of flowing fluid across their interstices.

This work therefore, seeks to investigate the impact of sudden enlargement and sudden contraction of moving fluid in porous metallic structure (stacked samples) using

Computational Fluid Dynamics (CFD) modeling and simulation coupled with 3D advanced imaging techniques.

1.2 Statement of the Research Problem

There are little or no published articles on Computational Fluid Dynamics (CFD) approach to study the contributory effect of sudden in pore- volume on the flow behaviour of high density porous structures using CFD approach coupled with 3D advanced imaging techniques Otaru *et al*., (2018b). This issue will be addressed in this study.

Porous metals are currently used as separation device in water purification and petroleum processing. Currently available porous materials are characterised by monodispersed pores with little or no insight into polydispersed pores or multi- layered porosity. This work will give an insight into such, numerically.

1.3 Aim and Objectives of the Study

The aim of this work is to represent the pressure gradient/pressure drop developed for a moving fluid across commercially available high-density porous metallic structures (Porvair^{TM}, Inconel^{TM} (Alantum^{TM}) and Recemat^{TM}) utilising X-ray computed tomography datasets. The aim of this work will be achieved with the following objectives;

1. 3D advanced imaging analysis via tomography datasets.
2. Numerically investigate the pressure drop across a 3D representative volume created from the tomography slices.
3. To investigate the effect of stacking samples, hence, sudden enlargement and sudden contraction on pressure drop.

4. Determination of permeability and form drag of the samples using Darcy-Dupuit-Forchheimer expression.
5. Analysis of the pore related parameter on the flow information.
6. Establish modeling confidence by validating with literature data.

1.4 Justification of the Study

1. Understanding the flow behaviour in porous metals could lead to the development of novel attributing structures capable of supporting/replacing materials for cutting down emissions.
2. This work will help in providing in-depth understanding into the flow information of single (or) stacked samples, and flow entrance and exit effects at the pore-level.
3. Accurate CFD modeling and simulation coupled with 3D advanced imaging techniques will provide an alternative way of cost reduction couple with a better understanding of flow behaviour at microscale level.

1.5 Scope of Work

The research work is limited to the combination of 3D advance imaging techniques and computational fluid dynamics (CFD) modeling and simulation to investigate the sudden change in pressure drop of airflow (velocity range from 0 – 6.0 $m.s^{-1}$) and flow information across commercially available high-density porous metallic structures and stacked samples using Comsol Multiphysics 5.2 software packages. The following boundary condition are considered for the work; inlet velocity ($v = v_0$), outlet pressure ($p = p_0$), no-slip velocity on the solid wall of the structures ($V = 0$) and symmetry boundary a lone the symmetry plane ($V = 0$)

CHAPTER TWO

2.0 LITERATURE REVIEW

Highly porous metals, otherwise referred to as metal foams, have been attracting a growing interest in the engineering world due to their low density, high porosity, good liquid and gas permeability, high surface area, and other unique properties (Banhart, 2014).

2.1 Porous Metals

Porous metals can be defined as cellular structure or a near-net or sponge- like shape of solid metals made up of a solid matrix also known as struts, with visual fascinating pores and pore openings. Porous metal structures are produced from various metallic materials such as aluminum, titanium, nickel, steel, copper, nickel, chromium and metal alloys (Xiao, 2013; Dalla Torre *et al*., 2014; Baloyo, 2016; Otaru, 2019).

Furthermore, porous metals are multi- functional materials, which offer a combination of varying properties characterised by high porosity (density) typically between the range of 75 and 95% (filled with air) and pore sizes between the range of 0.2 and 5.0 mm accounting for their high surface area and ultra- light materials, hence their usefulness for high pressure, load bearing and high-temperature applications materials (Jorge and Malcon, 2010; Xiao, 2013), while packed bed and bottleneck porous metal are characterised by low density with porosity range of 34 - 44% and 60 - 75% respectively Otaru *et al.*, (2018a).

Khayargoli *et al*., (2004) reported that metals foam are being produced since several decades, new metal foams with improved properties are constantly being introduced into the market and their use in new applications are expected to grow in the near future. Porous metals attract the attention of scientist due to their physical and structural properties in last century and also still receiving a growing audience in recent year (Ashby *et al*., 2000).

Considerable attention in both academia and industry is focused on their low density, relatively high specific strength, air and water permeability, and thermal and acoustic properties. Porous metals are generally classified into two namely; close-cell porous metal and open-cell porous metal.

Close-celled porous metallic structure also known as air-sealed porous metals are metal that consisting of voids that are not connected and are separated by the solid metal matrix (Otaru, 2019). Figure 2.1a present morphology of close-cell structure and is type of metal form that is usually used as structural materials, such as electromagnetic shields, impact energy absorbers and decoration materials for the construction industry (Xiao, 2013). Open-celled porous metallic structure (Figure 2.1b) on the other hand, are metals whose voids are interconnected, hence providing pathways for fluid flow (Ashby and Tianjin, 2003). They are commonly use as structures that interact with a fluid in processes such as heat exchange and storage as well as filtration, acoustic and vibration control, catalytic reactor and biomedical devices because of their high specific surface area (Dukhan and Ali, 2012; Zhao, 2012; Furman *et al*., 2013; Otaru *et al*., 2018b).

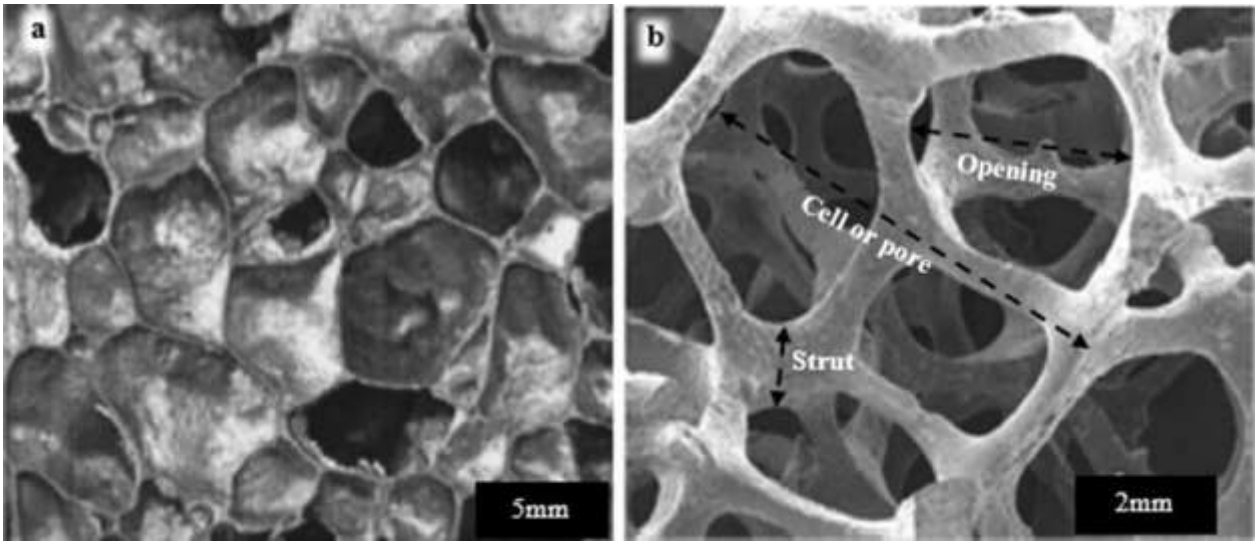

Figure 2.1a: Micrograph of a close-celled porous metallic structure (sourced Zhou, 2006; Otaru, 2019).
Figure 2.1b: Micrograph of an open-celled porous metallic structure (sourced Zhou, 2006; Otaru, 2019).

2.2 Production Methods and Techniques

There are a number of methods and techniques available to produce porous metals. Some of the production methods have been applied in industrial manufacture and new novel techniques are developed to achieve better properties and lower production cost. Some commercially available porous metals such as Porvair, Recemat™ and Alantum™ are classified as highly porous metals characterized by porosity between the ranges of 80 and 95% and can be produced by replication of an open-celled porous polymeric structures (Otaru, 2019).

2.2.1 Liquid state method

Metals in their liquid state are been transformed into porous metals using the following techniques:

2.2.1.1 Powder metallurgy technique (foaminal/alulight)

This technique is also known as the powder-compact melting process. In this process, the blowing agents (e.g. TiH_2or ZrH_2) are uniformly distributed and embedded into the powdered metal matrix (aluminum, zinc, brass, tin, gold, lead, alloys) by compaction resulting in a dense nearly- finished product; compaction can be done by rod-extrusion or powder rolling, is static or uniaxial compression method. After compaction, heat treatment at an extremely high temperature (near the melting point of porous materials) is carried out which causes the blowing agents to decompose and release gas which in turn leads to a significant expansion of the matrix (Banhart *et al*., 1999). It is important to note that, the extent of the melt expansion depends to a large degree on the melting temperature and precursor size from a few seconds to several minutes (Otaru, 2019). The advantage of this technique is that mass production of a highly porous cellular core with closed outer skin suitable for light weight and energy absorption applications can be achieved and a near-net shape can be obtained with porosity in the range of 60 - 90% (Banhart *et*, *al*. 1999; Baloyo, 2016). However, for a small-scale commercial production of porous metals by this technique, difficulty exists in the accurate control of the melt expansion during heat treatment; if the expansion is not limited, the resulting structure ends up with undefined shapes. Hence, process parameters need to be carefully controlled.

2.2.1.2 Investment casting technique

In this process, reticulated polyurethane foam is filled with a refractory molding material, after which it is cured and then the polymer foam is burnt out. The molten metal, which includes Aluminum, Copper and Magnesium alloys, is then casted into the resulting cavities, thus replicating the structure of the original polymer foam. After solidification, the mould material is removed leaving a highly porous metal having porosity within the range

of 80–95% porosity (Dukhan, 2013; Baloyo, 2016). Complex shapes can be gotten by pre-forming the polymer foam but difficulties arise in removing the mould material from the metal matrix.

2.2.1.3 Space-holder casting technique

The space-holder casting technique also known as replication casting process is yet another process used in the manufacturing of open-celled porous metals. This technique can be carried out in two ways:

1. The Use of Low Density Hollow Spheres: In this manufacturing route, a liquid metal (material) is poured into a metallic vessel consisting of hollow spheres of the desired shape after which it is allowed to solidify after mixing before compaction. The porous hollow sphere is then removed by dissolution in warm water or thermal degradation to leave porosity (Sharafat *et al*., 2006).
2. The Use of Organic/Inorganic Hollow Spheres: In this manufacturing route, liquid metals are cast around organic or inorganic hollow spheres (packed beds of salts or porogens. The granules can be removed by heat treatment or by leaching techniques to produce 'sponge like' metal foams. Then again, they could also remain in the metal matrix to produce closed-cell metal foams (Sharafat *et al*., 2006; Baloyo, 2016).

The advantage of space-holder or replication casting route is that the morphology of the pore sizes can be manipulated through the sizes of the space holders (salts or porogens) used and has complete effects on the foam porosity by controlling the porogens packing density. The sizes of the pore opening depend to a large degree on the applied differential gaps created by the hollow spheres. This implies that, larger pore openings signify lower

applied differential pressures while smaller openings indicate the presence of high applied differential pressures which forces the liquid melts into the spaces created by the porogens (salt). Such porous metallic structures made by this space- holder technique are referred to as "bottleneck" structures (Otaru, 2019).

2.2.1.4 Spray forming technique

In the spray forming technique also known as the Osprey process, the molten metal is atomized and sprayed onto a substrate; the droplet deposit and afterward solidifies (Banhart *et al*., 1999). The resulting open-celled metal foam formed possesses fine grain size with low oxide content; properties can be modified by injecting powders (oxides or gas producing powders) into the spray. The pore morphology, on the other hand is not uniform and as such its properties would not be uniform throughout the structure, it has a maximum porosity of 60% which is similar to that of (Fujibayashi *et al*., 2004).

2.2.2 Solid state method

Metals in their solid state can be transformed into porous metals using the following techniques:

2.2.2.1 Sintering of metal powder/ fibre technique

Metal powder/fibres such as Tin, Bronze and stainless steel can be compacted or moulded to shape and then sintered at an elevated temperature using this technique. The manufacturing process begins with the mixing of metal powders (tin, gold, lead, and alloys) with a blowing agent, after which the mixture is then compacted to yield a dense semi-finished product (Banhart, 2014). This compaction can be achieved using any technique in which the blowing agent is embodied into the metal matrix without any notable residual

open porosity. Some compaction methods that could be used in this technique includes; uniaxial or isostatic compression, rod extrusion or powder rolling.

After compaction is complete, the next step is heat treatment at elevated temperatures near the melting point of porous metals which aids the homogenous distribution of the blowing agents within the dense metallic matrix and hence the decomposition of the blowing agents thereby releasing gas and forces the melt to expand significantly forming its highly porous structure (Otaru, 2019). The time required for full expansion depends on the temperature and size of the precursor ranging from a few seconds to several minutes. The resulting open-cell metal foam formed has a relatively low porosity within the range of 20 – 50% (Baloyo, 2016). This technique has the advantage of producing a high porous cellular core with closed outer skin suitable for lightweight and energy absorption applications. However, it is important to note that small-scale commercial production of porous metals using this route currently exists due to the difficulty in accurate control of the melt expansion during heat treatment at elevated temperatures. (Zhao *et al.*, 2005; Lee *et al*., 2006; Zou *et al*., 2008; Otaru, 2019)

2.2.2.2 Slurry foaming technique

In slurry foaming, the slurry consisting of the metal powder, blowing agents and reactive additives is prepared and poured into a mould. After this is done, it is then heated up at a high temperature causing the slurry to become viscous and expand. The expanded slurry is dried and the resulting metal foam is sintered to boost the strength. The open-celled metal foam formed has a large porosity range ≤93 (Gladysz and Chawla, 2015; Baloyo, 2016).

2.2.2.3 Space-holder technique

Highly porous titanium, copper, stainless steel and nickel-based super-alloys with porosity within the range of 60–80% can be manufactured using space-holder technique. Some of the types of space-holders currently used are; ceramic particles, polymer grains, salt or hollow spheres. In this technique, the first step to take involves the mixing of the space-holder with the metal powder with the addition of a suitable solvent/binder. This mixture is then pressed and the space-holder removed by thermal treatment after which the compacts are sintered in a vacuum atmosphere to produce metal foams with comparatively high strength (Bram *et al*., 2000). Large porosity range is achievable using this technique.

2.2.3 Vapour state method (vapour deposition)

Basically, all metals in their vapour state can be transformed into porous metals via vapour deposition technique. The following steps are carried out during the transformation; the first step is to place a cold solid precursor structure (e.g. polyurethane) in a vacuum chamber where the metal vapour is produced. The metal vapour then condenses onto the precursor, coating its surface; the thickness of the coating depends on the vapour density and time or period of exposure. The polymer formed is then removed from the metal matrix by either thermal or chemical treatment. The resulting open-cell porous metal formed has a very high porosity as only high porosity range is achievable (92 - 95%) and the pore morphology can be tailored (Ashby *et al.*, 2000; Yang *et al*., 2008; Baloyo, 2016).

2.2.4 Ionic state method (electro-deposition)

Porous metals can be transformed from their ionic state by electro-deposition technique. In this technique, the polymer foam precursor is coated with a conductive layer by dipping into conductive slurry or by cathode sputtering. The metal can then be electrically deposited

onto the electrically conductive polymer foam after which the polymer foam is removed by thermal treatment yielding a porous metal with hollow struts. Some examples of metal foams manufactured using electro-deposition technique includes Nickel, Ni–Cr alloys and Copper with high porosity in the range of 93 – 98% (Lu and Chen, 2014). Just as in vapour deposition method, pore morphology can be tailored.

2.3 Pore-Structure Characterization

Porous metals are opaque to visible light that limits the measurements of their intricate morphology often made up of stubby pores connected by narrower throats. The opacity prevents also the direct visualization of all the important phenomena related to the flow of multiphase fluids in the complex porous morphology. Among the tomography imagining techniques, the X-ray computed tomography is the one with highest spatial resolution, good penetrating capability and thus it is the most suited for the morphological reconstruction of porous media samples with micrometric throats (Piller *et al.*, 2014).

Advanced imaging techniques working from X-ray computerized tomography (CT) data has been used to enable assessment of the structural properties (pore sizes, openings, roundness and volume) of the porous metals at micro scale level. X-ray tomography images or datasets have been used to reliably characterise the pore structure-related parameters of high-density porous metallic structures such as Alantum450µm, Alantum1200µm, Recemat1116 PPI, Recemat1723 PPI and Porvair7 PPI. In the modelling work, great caution was taken to confirm the reliability and accuracy of the models, investigating the effects of the parameters selected for the models and comparing to experimental data available in the literature (Otaru, 2018).

Pore structure characterization of these samples via tomography datasets from literature has shown that pressure drop depends both upon the fluid properties and on the permeability of the porous metal, which was influenced by the porosity, cell size, and the morphology of the pores and the pore network (Oun and Kennedy, 2014). The pressure drop across these highly porous commercially available metal foams can be improved by increasing the surface area of the materials either by compression or using the salts coating replication casting techniques. X-ray micro-CT scans are employed to obtain accurate digital representations of the foam samples and determine porosity, specific surface and mea n pore size directly from the tomography datasets.

Tomography datasets are defined as sets of grey values Ψijk uniformly distributed in a Cartesian grid with spacing h. The scanning process generates stacks of Nz8-bit grey-scale images of $Nx \times Ny$pixels each, corresponding to $Nx \times Ny \times Nz$voxel. The 3-D matrix of grey values can be regarded as a smoothed representation of the pore and solid space, respectively, with a smoothing kernel of size h, corresponding to the scan resolution. The pore and solid spaces of porous metals have distinct optical densities, which are associated with local X-ray absorption coefficients, reflecting different phases (solid or fluid) within the material. The process of digitally identifying these phases and partitioning them into disjoint segments is referred to as segmentation. However, it is often necessary to perform image enhancement operations before segmentation. The resulting images obtained from the CT scanning process are not sharp enough and can present significant light scattering and noise. These issues are corrected prior to segmentation by applying image intensity adjustments (to enhance contrast), unsharp masking (sharpens the edges) (Sheppard *et al.*, 2004; De Carvalho *et al.*, 2017) and 2-D median filtering (to reduce noise). Due to the

nature of the images, it has been noticed that careful selection of the image adjustment parameters is necessary, since it can greatly affect the outcome of the volume re ndering procedure. The image enhancement was followed by segmentation. The solid-pore interface is determined by defining a grey- value threshold level, denoted as Ψ_0. All pixels in the input image with a value greater than or equal to the threshold is replaced with the value **'1'** for the solid space and value **'0'** for the pore space, yielding a set of binary values $\Psi(\text{bin})ijk$. The global grey-value threshold level $\Psi 0$ is determined using Otsu's method (Otsu, 1975; De Carvalho *et al.*, 2017). This process yields a continuous representation of the solid-pore interface, represented as an iso-surface, $\Psi(\mathbf{x}) = \Psi 0$. Therefore, the pore indicator function can be written as:

$$3(\mathrm{X}) = \begin{cases} 1, & \text{If } \mathrm{T}_{\mathrm{ij}k}(x) < \mathrm{T}_0 \\ 0, & \text{If } \mathrm{T}_{\mathrm{ij}k}(x) \geq \mathrm{T}_0 \end{cases} \tag{2.1}$$

And is used to convert the grey-scale matrix into a 0/1 binary matrix. Open-cell metal foam commonly has hollow struts due to their manufacturing process, constituting a number of disjoint pore regions not relevant to fluid flow. Therefore, the largest subset of the pore space is computed by the use of a flood fill operation. This largest subset constitutes the main pore space. The remaining smaller disjoint pores are artificially closed by converting their voxel to 1 (solid), since they are irrelevant for the flow (De Carvalho *et al.*, 2017). The tomography datasets can be used for direct computation of macroscopic morphological parameters such as porosity, specific surface, mean pore and strut diameter and MGRV size for each sample.

2.3.1 Porosity

The porosity, φ, is determined from the tomography datasets by counting the number of voxel in the solid phase and dividing by the total number of voxel from the binarized datasets, namely:

$$\emptyset = 1 - \frac{\sum_{K=1}^{N_X} \sum_{K=1}^{N_Y} \sum^{N_Z} T_{(\text{bin ijk})}}{N_X \times N_Y \times N_Z} \quad (2.2)$$

The total porosity accounts for the pore space within the solid foam struts, whereas the effective porosity accounts for the main pore space only. In the work of Oun and Kennedy (2014), mercury intrusion porosimetry (MIP) was used to determine the total porosity of the Alantum 450-µmsample, which showed a value of 0.8133, presenting a relative error of less than 1% when compared to the tomography dataset. This result agrees with data from Lee *et al*., (2010), which reports a CT-computed porosity value of 0.8214 for the Alantum 450-µm foam and that of Otaru (2018), which reports a porosity value of 0.8354. From literature, the value of porosity for Alantum1200µm was given as 0.9062 and that of Recemat 1116 is 0.8981 the total porosity value of 0.8899 for the Recemat1723 computed from the tomography dataset compares well against total porosity values in the range of 0.89–0.90 reported by Medraj *et al*., (2007), where several samples of the Recemat1723 were analyzed. Finally, the value of porosity for Porvair 7PPI was given to be 0.8969 (0taru, 2018). The fraction of unconnected pore space was shown to be generally quite small (< 1%) for all foam samples (De Carvalho *et al.*, 2017).

2.3.2 Specific surface

The specific surface is defined as the solid-pore interface surface area per unit volume and is determined by applying the Cauchy–Crofton theorem using a MATLAB Broutine. The

total specific surface also accounts for the solid-pore interface area within the hollow struts, whilst the effective surface area accounts for the solid-pore interface area in the main pore space only. As general trend, the specific surface increases with decreasing pore diameter. The difference between total and effective specific surface values are more significant in samples with larger pore size, where the unconnected pore space inside the struts is better captured by the tomography scans.

2.3.3 Mean pore and strut size

The pore space of high density porous metals can be characterized by means of a pore size distribution. The pore size distribution is determined from the tomography samples by computing the opening size distribution. Opening is an operation of mathematical morphology, consisting of an erosion followed by a dilation using the same structuring element (SE), thus eliminating all geometrical features smaller than the current SE. Morphological opening was carried out by sequentially inscribing spherical SEs of increasing diameter in the pore space of the tomography datasets and counting the remaining number of (pore) voxel, until no more voxel are left. The opening size distribution is obtained by relating the number of remaining voxel with each increase in SE diameter. Maire *et al*., (2007); Petrasch *et al*., (2008) found that the cubical subsets of the original tomography datasets were used for determination of the pore size distribution due to heavy computational costs associated with such operations. Table 2.1 shows some experimental result of Alantum, Recemat and Porvair samples and the report also show that the permeability is influence by geometrical structure parameter i.e., pore diameter and porosity.

The mean pore diameter, d_p is calculated as:

$$dp = \frac{\int_0^{\infty} d_{SE} f(d_{SE}) \mathrm{d}d_{SE}}{\int_0^{\infty} f(d_{SE}) \mathrm{d}d_{SE}} \quad (2.3)$$

Where, d_{SE}= Structural Element Diameter and $f(d_{SE})$ = Opening Size Distribution.

Table 2.1: Experimental Pore Related Parameter and permeability (Otaru, 2018)

Sample	Pore Diameter D_p(mm)	Porosity ε (%)	Permeability k_0 $(m)^2$
Alantum 450µm	0.45	83.54	1.22 E-09
Alantum 1200µm	1.23	90.62	1.53 E-08
Recemat 1116PPI	2.45	89.81	6.67 E-08
Recemat 1723PPI	1.86	80.96	1.62 E-08
Porvair 7PPI	1.47	89.69	2.74 E-08

2.3.4 Tortuosity

Tortuosity characterizes the fluid flow path through a porous medium. Tortuosity is the ratio of the average pore length to the length of the porous medium along the major flow axis. A large tortuosity value indicates a windier channel for fluid flow, and is often linked to smaller permeability value and higher form drag coefficients. It was reported that with increased porosity, the flow becomes less tortuous since more channels are available for fluid flow (Sun *et al.*, 2013).

2.4 Reynolds Number

Reynolds number (N_{Re}) is often used for Newtonian fluids to describe their viscous flow behavior. Reynolds number is dimensionless and can be described as follows:

$$N_{Re} = \frac{pVL}{\mu} \tag{2.4}$$

Where p is the fluid density (Kg/m^{-3}), V is the velocity ($m.s^{-1}$), μis the fluid viscosity and L is the length of the material (m) White (2009). At low N_{Re} range, the flow is in the laminar region (Darcy's regime) where the inertial effects are very small. As the Reynolds number increases, a transition occurs where the flow becomes unpredictable, and both laminar and turbulent flows are present. The flow enters the Forchheimer regime as it becomes turbulent at very high Re range due to greater inertial effects. Numerous of research has been conducted in the past to evaluate the N_{Re} values of the flow regimes for different flow systems.

For instance Kececioglu and Jiang (1994) suggested that Darcy's law only applies at extremely low flow velocities where the Reynolds numbers is in the range of 0.3 – 0.7. Farkas *et al.*, (1999) investigated the validity of Darcy's flow at low flow rates using liquid chromatography and concludes that Darcy's Law only applied to low flow velocities in the range of $N_{Re} = 1 \times 10^{-6}$ to 1×10^{-4}. Cornel and Katz (1953) found that for gasses flow the flow regime was laminar at $N_{Re} < 0.08$ where the pressure drop was directionally proportional to the flow rate at $0.08 < N_{Re} < 8$, the transition region occurred at $N_{Re} > 8$, the flow became turbulent. Comparably Ergun observed that the critical Re of 3 – 10 was found for turbulent gas flow through packed beds. Likewise Hassanizadeh and Gray (1987) suggested that N_{Re} – 10 is the critical value for non-Darcy flow behavior due to the increase

of the microscopic viscous force at high velocities. Numerical models were also used to predict the critical N_{Re} where the flow transit to turbulent flow from laminar Blick and Civan (2013) used capillary – onfice modeling to simulate fluid flow in the porous media and reported that the critical N_{Re} is 100 for non-Darcy behavior Du Plesis and Masliyah (1988) on the other hand used a representative unit cell model and calculated the critical N_{Re} to be between 3 and 17. In contrast, Thauvin and Mohanty (1998) used a network model to simulate the porous media using the pore throat radius and found the N_{Re} to be 0.11.

2.4.1 Flow regime in porous media

Not every flow through porous media is laminar. High speed flow (high Reynolds number) through porous media can occur and lead to the onset of turbulence within the pore space. This is even more likely if the interstitial fluid is a gas and if the porous medium is coarse (high porosity). The Reynolds number based on the mean pore diameter Re_p is commonly employed to characterize flow through highly porous media and is defined as:

$$Re_p = \frac{puDdp}{\mu} \tag{2.5}$$

With dp as the mean pore diameter and U_D as the Darcian velocity, this is defined as the average superficial velocity computed as

$$U_D = \frac{Q}{A_f} \tag{2.6}$$

Where Q is the volumetric flow rate and A_f is the cross-sectional flow area. There are essentially four types of flow regime in porous media namely; (1) Darcy or Creeping flow

regime (Re_p <1); (2) Forchheimer flow regime (K Re_p < 150); (3) Post-Forchheimer flow regime (150 < Re_p < 300) and (4) fully turbulent flow regime (300 < Re_p) (De lemos, 2012, Pedrs and Lemos 2001).

2.5 Fluid Transport in Porous Structures

The part of fluid mechanics that deals primarily with fluid dynamics is termed fluid flow. Fluids are categorized into gases and liquid and when subjected to a motion of unbalanced forces it is called fluid flow. A typical example of this is the flow of water or oil from an overhead tank. The superficial velocity (Vs) of the fluid is very high on the top and low at the bottom of the tank with unbalanced gravitational force (g) enabling a continuous flow of fluid. The defining characteristics of this fluid mirror its properties and how it moves Otaru (2019). These properties can be compressible (fractional change in volume due to density variation at different temperature especially for gases) or in. compressib le (no change in volume especially for water), steady (time-dependent) or unsteady (time – independent) rotational or non-rotational, viscous (shear stress directly proportional to fluid velocity) or Non-viscous, Newtonian (Viscous stress linearly proportional to local strain rate) or have ability to resist deformation by tensile or stress known as a Non-Newtonian fluid. The numerical study of this fluid flow is known as computational fluid dynamics (CFD) and is well adopted in the field science and engineering to mimic flow behavior even in the pavaty of experimental or measured data. The study of fluid flow is governed by the equation of continuity and momentum or Navier – stoke equation (Baloyo, 2016).

2.5.1 Fluid flow in porous media

Permeability is an important attribute of open-cell porous metals which greatly influences the convective heat transfer properties. Permeability describes how easy a fluid can flow

through porous material. Simply, permeability refers to the conductivity of a porous medium with respect to fluid flow. Furthermore permeability is dependent on the structural nature of the porous material that is, its porosity, the distribution and connectedness of the pores and pore size (Baloyo, 2016). The most common theory used to evaluate fluid transfer in porous media is Darcy's Law.

$$\frac{\Delta p}{\Delta L} = \frac{\mu Q}{KA} \tag{2.7}$$

Where ΔP is the pressure drop (Pa) ΔL is the flow length (M), K_0 is the permeability (m^2), μ is the viscosity of the fluid (Pa.s), Q is the fluid flow rate ($M^3 S^{-1}$) and A is the cross sectional area to fluid flow. Darcy's law was formulated in the late eighteenth century while investigating water flow through sand filters for water filtration. However, it was not until recently that it was applied to other porous structure in the nineteenth century. Darcy's law was modified several times to fit different application and condition. For instance adapting Darcy's Law to describe the flow of incompressible fluids leads to.

$$V = \frac{K (P_{out} - P_{in})}{\mu L} \tag{2.8}$$

Where V = Q/A is the apparent velocity also known as Darcian velocity, Pin is the fluid's inlet pressure and Pout is the outlet pressure (Pa) for compressible fluids like air. Darcy's Law can be revised to.

$$V = \frac{K (P^2_{out} - P^2_{in})}{2\mu L P_{out}} \tag{2.9}$$

Various researchers found that a deviation from the linear Darcy's Law arises when the fluid flow velocity is increased White (2009) explained that this phenomenon is due to the

inertial effect followed by turbulent effects as a result. Darcy's Law was mod ified to account for the inertial effects at high flow velocities. The modified non- linear Darcy's Law common known as Forchheimer equation, describes the steady – state flow as follows:

$$\frac{P}{\Delta L} = \frac{\mu v}{K} + pcv^2 \qquad \text{Eqn 2.10}$$

Where C is the form drag coefficient known as Forchheimer's factor, De Carvalho *et al.,* (2017)

2.5.2 Turbulence modeling

De Carvalho *et al.,* (2017) also reported that investigating the flow regime is expected to be predominantly within the turbulent flow range. Hence a model is required to account for the turbulence within the pore space most turbulence models rely on what is referred to as the Reynolds averaging technique. As turbulence is characterized by random fluctuations, the instantaneous Navier-stokes equation can be decomposed into mean (ensemble- average or time averaged) and fluctuating component. In this way, the pore velocity components using Einstein motion are decomposed as:

$$U_i = \bar{U}_i + U^i{}_i \qquad (2.11)$$

Where $\bar{U}_i$ and $U^i{}_i$ are the mean and fluctuating velocity components respectively, Likewise this decomposition can be applied to other scalars quantities.

$$\varphi = \varphi_i + \varphi^i \qquad (2.12)$$

Where φ denotes any scalar such as pressure, energy or species concentration De Carvalho *et al.,* (2017). Applying this approach to the Instantaneous mass and momentum equations

and time averaging hem (and dropping the over bar on the mean velocity u) yields the Reynolds average Navier –stokes (RANS) equation.

2.6 Computational Fluid Dynamic

Computational Fluid Dynamics or CFD is a branch of Fluid dynamics providing a cost effective means of simulating real flows by numerical solution of the governing equation such as Navier-Stoke equation (Abdulnaser, 2009). CFD can also be described as the analysis of systems involving fluid flow, heat transfer and associated phenomena such as chemical reactions by means of computer-based simulation. CFD involves approximating partial differential equations as simple linear relations. The domain of interest is divided into a finite grid, commonly referred to as a mesh. As the mesh becomes finer, its elements become smaller and closer together, and the approximation will converge to the actual solution. Such a method is computationally intense, and therefore is best suited to be conducted using software. A number of CFD software packages and meshing utilities exist and are available for purchase. The techniques are very powerful and span a wide of industrial and non-industrial area. Some examples are:-

1. Aerodynamics of aircraft and vehicles: lift and drag
2. Hydrodynamics of ships
3. Practically unlimited level of detail results. (Abdulnaser, 2009)

2.6.1 Computational mesh

One of the vital components in the solution of the non linear PDE is computational mesh. The finer or denser a mesh is, the more numerically accurate the computation is but more time is taken for the computation to be completed (Zuo, 2005). Mesh densities can be

varied across any particular geometry so that particular regions that require higher numerical accuracy can have a denser mesh and regions that do not necessitate high accuracy can have a coarse mesh, thus improving the accuracy in important areas while still minimizing the computational time required for the calculations (Abdulnaser, 2009).

2.6.2 Stages involve in computational fluid dynamics

Three stages are involved in carrying out Computational Fluid Dynamics:

1. Pre-processor: pre-processing consist of a flow problem to a CFD program by means of an operator- friendly interface and subsequent transformation of this input into a form suitable form suitable for use by the solver. The user activities at the pre-processing stage involve:

    i. Definition of the geometry of the region of interest i.e. the computational domain.

    ii. Grid generation; the sub-division of the domain into a number of smaller, non-overlapping sub-domains: a grid (or mesh) of cells) or control volumes or elements).

    iii. Selection of the physical and chemical phenomena that need to be modeled

    iv. Definition of fluid properties.

    v. Specification of appropriate boundary conditions at cell which coincide with or touch the domain boundary.

2. Solver

There are three distinct streams of numerical solutions techniques: finite difference, finite element and spectral method. In outline, the numerical methods that form the basis of the solver perform the following steps:

i. Approximation of the unknown flow variables by means of simple functions.

ii. Discretisation by substituting of the approximation into the governing flow equations and the subsequent mathematical manipulations.

iii. Solution of the algebraic equations.

2.6.3 Discretisation methods

2.6.3.1 Finite difference method (FDM)

This is the simplest procedure used to derive the discrete form of a different equation. It is applied especially on uniform grids; it also requires high degree of mesh regularity. The mesh needs to be setup I structured in a way where mesh point should be located at the intersection points of families of rectilinear curves (Dixit, 2014). This method is limited for practical application and only very small engineering codes rely on this method.

$$\frac{dQ}{dt} + \frac{dF}{dx} + \frac{dG}{dy} + \frac{dH}{dz} \qquad (2.13)$$

Where Q is the vector or conserved variables, F, G and H are the fluxes in the x, y, and z directions.

Zhou, (1993) reported that FDM is used to solve linear and non linear, time independent and dependent problem, and can also be used to resolve problem having different boundary

shape, many type of boundary condition and for a point with different number o f materials. Within the period of 1950 – 1970s, FDM was the most widely utilized numerical solution approach for practical problem. As a result, several numerical solution approaches for solving partial differential equations arose as a result of the availability of high-speed computer with large-scale storage capacity Zhou, (1993).

2.6.3.2 Finite element method (FEM)

The finite element method is based on the so called method of weighted residuals. This is a powerful method of solving partial differential equations which was developed between 1940 and 1960, mainly for structural dynamics problem. This method has a distinct advantage over the finite difference because it can handle complex arbitrary geometries as it can be easily applied using irregular grids of various shapes (Abdulnaser, 2009). Dixit (2014) describe the FEM for a linear differential equation as follow:

$$\boldsymbol{Lu} + \boldsymbol{q} = 0 \tag{2.14}$$

Where $\boldsymbol{u}$ denoting the vector of primary variables of the problem, as coordinates function, $\boldsymbol{L}$ is the differential operator and $\boldsymbol{q}$ is the vector of known function.

FEM is also a general method because is successful in using Multiphysics analysis (electromagnetic and structural analysis). It is significant to other method to other method because it can combine various types of function to estimate solution within each element. This is generally referred to as mixed formulation and it is simple in FEM but complicated and uncertain for other Dmitri and Jari (2014); Cadence (2020).

2.6.3.3 Finite volume method (FVM)

FVM can be viewed as a special case of weighted residual method where the weighting function takes the form $W_i = 1$. A number of weighted residuals equations are generated by dividing the solution into sub-domains called control volumes and setting the weighting function to be unity over the control volumes one a time and zero elsewhere.

In finite volume method, the governing partial differential equations (typically Navier-stokes equations, the mass and energy conservations equations) are recast in a conservative form, and then solve discrete volumes (Abdulnaser, 2009). The geometrical flexibility of finite element method and finite volume method are the same Erik (2009)

2.6.4 Grids

Grid or mesh is defined as smaller shapes formed after division of geometric domain. Mesh or grid can be in 3-dimension or 2-dimension. There are three types of grid; structured grids, unstructured grids and Block structured grids (Zuo, 2005).

2.6.4.1 Structural grids

The simple one is structured grid. In this type of grid all nodes have the same number of elements around it. This type of grid is only for simple domain. They can easily be described and stored easily (Abdulnaser, 2009).

2.6.4.2 Block structured grid

In this type of grid the domain is divided into different regions. Each region has different type of mesh structure. It is also possible that different co-ordinate system can be used for different regions. This makes fluid far more flexible. This also makes the refinement in the region where the geometry is to be captured more precisely (Abdulnaser, 2009).

2.6.4.3 Unstructured grid

In complex geometries it is logical to use large number of blocks and therefore it leads to unstructured grid. These are widely accepted in CFD because this gives far more flexibility and computer resources are efficiently utilized. The advantage of unstructured grid is that mesh can be refined wherever needed (Abdulnaser, 2009).

2.6.5 Boundary conditions

The most integral part of any computational fluid dynamics problem is the definition of its boundary conditions. Different types of boundary conditions are used in CFD for different conditions.

2.6.5.1 Inlet boundary conditions.

The inlet boundary condition is common and specified mostly where inlet flow velocity is known.

2.6.5.2 Outlet boundary conditions.

In outlet boundary conditions, the distribution of all flow variables needs to be specified at outlet boundaries mainly flow velocity. This type of boundary condition is common and specified mostly where outlet velocity is known. The flow attains a fully developed state where no change occurs in the flow direction when the outlet is selected far away from the geometrical disturbance. In such region, an outlet could be outlined and the gradient of all variables could be equated to zero in the flow direction except pressure which is presented in table 2.2 below.

Table 2.2: Summary of common boundary conditions for fluid flow **(**Hesketh, 2008; Otaru, 2018)

Boundary	Boundary Conditions	Equation	Use
Wall	Sliding Wall	$v = v_w$	Used to specify the velocity of a moving wall.
	No-slip (default)	$v = 0$	Zero velocity at the wall.
Inlet	Velocity	$v = v_0$ or $v = -nv_0$	To specified constant velocity or a defined velocity by an equation as v = a(1-($\frac{r}{R}$)^2). Where n is a unit vector normal to the surface.
	Pressure, no viscous stress	$p = p_0$	Use to describe fluid inlet perpendicular to the boundary
Outlet	Velocity	$v = v_0$ or $v = -nv_0$	Be careful not to over-specify.
	Pressure, no viscous stress	$p = p_0$	Used to describe fluid outlet perpendicular to the boundary
Symmetry	Slip/symmetry condition	$v.n = 0$	Used to specify no velocity perpendicular to a surface or an area. For example, fluid flow in a 3D porous object, the inlet and outlet may be velocity or pressure flow while the other sides are treated as symmetry
	Normal flow/pressure or 'straight – out' BC	$p = p_0$ &$v.t = 0$	Used for fully developed flow perpendicular to the area.
	Outflow/Pressure BC	$p = p_0$	Used for known pressure

2.6.5.3 Temperature dependent properties.

According to Yashar (2015), various combinations of the model have been tried and their advantages were compared. During each of the stages in the model development process, some simplifications were proposed and they have been checked with a similar numerical model that was less simplified compared to the physical furnace setup. When comparing to the comprehensive model, if the simplified case could predict the velocity profiles and temperature with an error percentage of 5% or lower, it would be marked as an acceptable model and would replace the more complex model for the next iteration of comparison.

The first type of models developed were laminar steady state flows inside the 3D tube furnace with constant density, viscosity and thermal conductivity. It was observed that due to the lack of temperature dependent properties, these models output data similar to a plug flow problem, in which a fluid flows in a tube with fully developed velocity and temperature profile. Therefore, these models cannot show the change in density (buoyancy effects). The second type of models developed was using Bossiness approximation with a given constant density. The Bossiness model should not be used if the temperature differences in the domain are large. In addition, it cannot be used with species calculations, combustion, or reacting flows. In other words this is a good approximation for a case which is nearly incompressible. The third type of models has temperature dependent properties. Since these models have temperature dependent viscosity and thermal conductivity, they manage to demonstrate buoyancy and flow shear effects, and thereby gives the most complete solution. Temperature dependent properties were modeled using piecewise linear approximation Yashar (2015).

2.7 Sudden Enlargement and Sudden Contraction in Pipe

The flow of fluid across an enlargement (increase in pipe diameter) results in a decrease in velocity and consequently, a pressure rise while flow across a contraction (decrease in pipe diameter) results in an increase in the velocity and consequently, a pressure drop greater than the value for the equivalent straight pipe (Azzopardi, 2011). He also reported that the energy dissipation caused within the region does not mean that pressure drop is converted to kinetic energy in sudden contraction or kinetic energy is converted to pressure rise in sudden enlargement, therefore, reversible and irreversible components must be considered in pressure drop.

Researchers also investigated fluid flow across sudden enlargement and contraction because indentifying flow behaviour across this geometrically simple fitting could enhance the knowledge of flow across more complex fitting, McNeil and Morris, (1995); Veruscha, (2004).

CHAPTER THREE

3.0 MATERIALS AND METHODOLOGY

3.1 Material

Table 3.1: list of materials

S/N	Sign	Samples	Sources
1	A	Inconel 450µm	Alantum™
2	B	Inconel 1200µm	Alantum™
3	C	RCM-NCX 1116 PPI	Recemat™
4	D	RCM-NCX 1723 PPI	Recemat™
5	E	Porvair 7PPI	Porvair™

Table 3.2: list of equipments

S/N	Equipment	Description
1	Comsol Multiphysics Version 5.2.	Software
2	Synopsys-Simpleware™	Software.
3	Computer system (laptop)	Folio 9470m EliteBookhp, Windows 10, 8GB RAM, 512 ROM
4	X-ray CT Machine	AZeiss Xradia Versa XRM-500 UK.

3.2 Tomography Datasets Acquisition

The research methods used in this study involved the acquisition of high-density porous metals, 3D image reconstruction and processing, meshing and computationally resolving fluid equations. AZeiss Xradia Versa XRM-500 3D X-ray CT system was used to acquire tomography datasets of Porvair 7PPI, Inconel 450 µm, Inconel 1200µm, Recemat RCM-NCX 1723 and Recemat RCM-NCX 1116 porous metallic structures with voxel dimensions ranging from 12 to 26 µm. The Scan IP module within Synopsys-Simpleware^{TM}, a 3D advanced image processing tool and model generation software package, was used to create a 3D volume and 3D representative volume element (RVE) whose pore volume fraction differed by ±2% from the original samples. The RVE pore volume fraction of individual sample was meas ured in the ScanIP by taking a Bolean inversion of the processed RVE structure (i.e. converting the structure phase to fluid phase) before measuring the volume fraction of the 3D RVE model.

With knowledge of the materials density, measures of the samples weight were done with a weighing scale to achieve the materials volume and nominal porosity of the "real" samples. A measure of the accurate representation of the processed 3D RVE was achieved through global thresholding and segmentation of the high- intensity grey scale values (high-density light areas) in the images whilst pore size was measured through use of the watershed segmentation algorithm of the 3D fluid volume. In addition, pore connectivity ("windows") and ligament thickness and sample surface area were measured using in-built statistical tools within the ScanIP. Figure 3.1 presents a sequential flow chart showing the 3D advanced imaging of the raw sample to 3D reconstructed RVE. Aside from the processed tomography data, 3D model printout of the skeletal phases of the porous materials were

also used (scaled, 1:10) to confirm the reliability of the measured pore-structure related parameters obtained from ScanIP with visible pore network and ligament topologies.

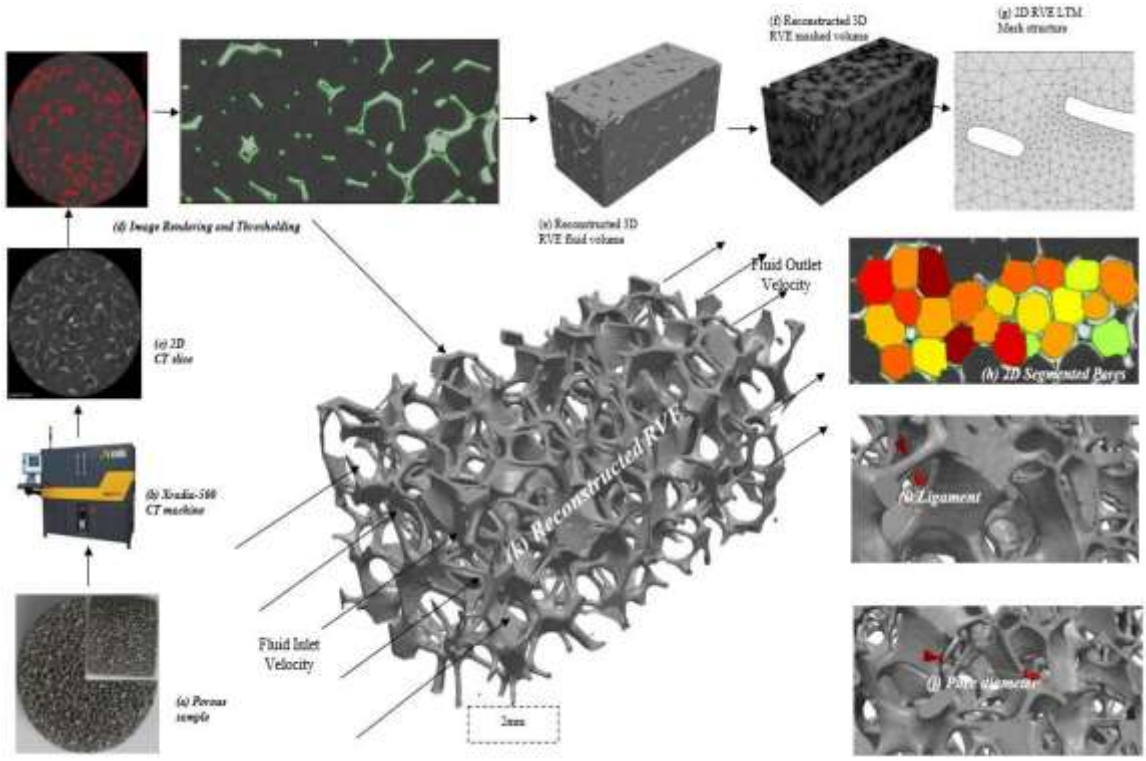

Figure 3.1: Representation of the image reconstruction via computed tomography (a) Porous sample (b) An AZeiss Xradia Versa XRM-500 3D X-ray CT microscope instrument (c) High- resolution 2D computed tomography slice data (d) Image rendering and thresholding (e) 3D reconstructed representative volume element (RVE Fluid) (f) 3D reconstructed RVE meshed volume (g) 2D LTM mesh structure (h) 2D segmented pores(i) 3D RVE Ligaments (j) 3D RVE pore diameter and (k) 3D reconstructed RVE skeletal phase of Porvair 7PPI porous structure.

3.3 Methodology

The chapter presents the method employed in carrying out the 2D and 3D CFD modelling and simulation of five commercially available high-density porous metallic structures and the hybrid/stacked samples with a focus on the pressure gradient/pressure drop developed for airflow across these metals samples in the Darcy-Forchheimer-Turbulence regime. Computational fluid dynamics (CFD) simulation of air flow through these porous structures was performed by solving the steady – state compressible Stokes, Navier Stock and Spalart-Allmaras TRANS k-ε model on a meshed fluid domain within a representative volume element(RVE), using the Single-Phase flow module in COMSOL Multiphysics 5.2. Meshing and mesh dependence study was also carried out on these samples in order to obtain an accurate and comprehensive information on the velocity and pressure gradients developed across the porous structures as well as the permeability and form drag for each sample. Figure 3.2 show steps below

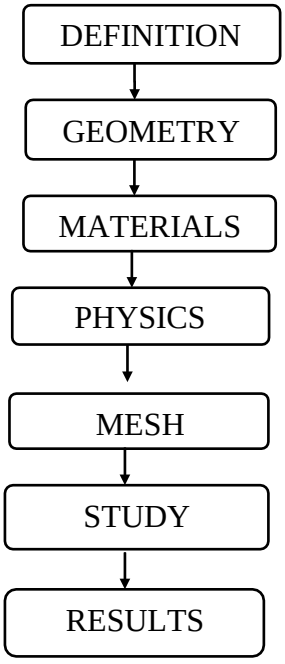

Figure 3.2: The steps for modelling and simulation in the Comsol Multiphysics Software Version 5.2.

3.3.1 Model definition

The model definition is carried out in 4 steps:

1. Creating a new model by selecting the Model Wizard which helps to set up the space dimension, physics and study type as shown in figure 3.3:

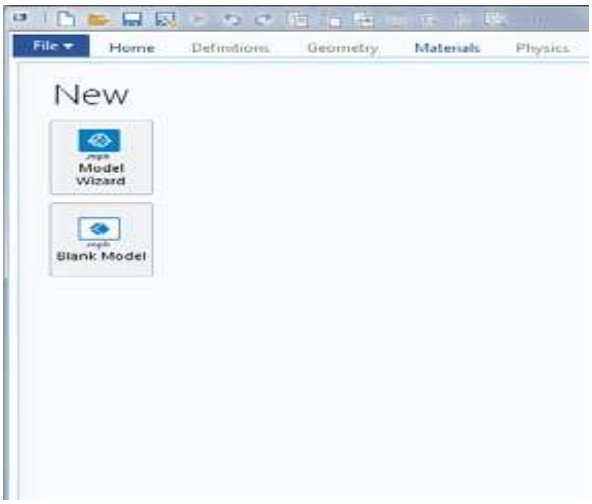

Figure 3.3: Selection of new model wizard of CFD (Comsol Multiphysics Software Version 5.2.)

2. Figure 3.4 present the selection of the space dimension for your model component(2-D)

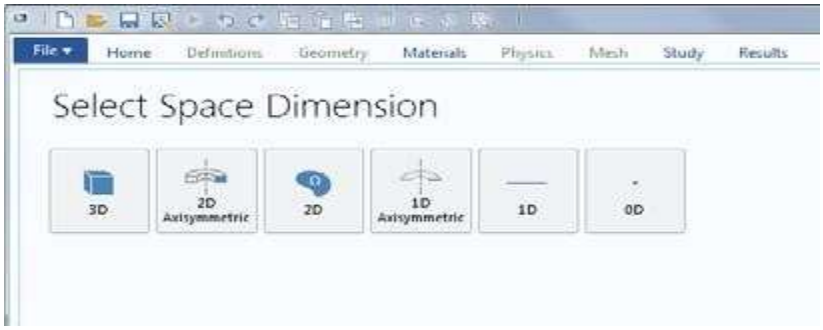

Figure 3.4: Space dimension selection of CFD

3. Add the physics interface for the computation. In the **Select physics** tree, select **Fluid Flow>Single-Phase Flow>Creeping Flow** shownin figure 3.5**.** (Comsol Multiphysics package). The process of fluid flow in this study is single-phase-flow because it deals with only air as a material for the current research work. Creeping flow (Darcy regime) is type of flow that have very low velocity with (N_{Re}< 1).

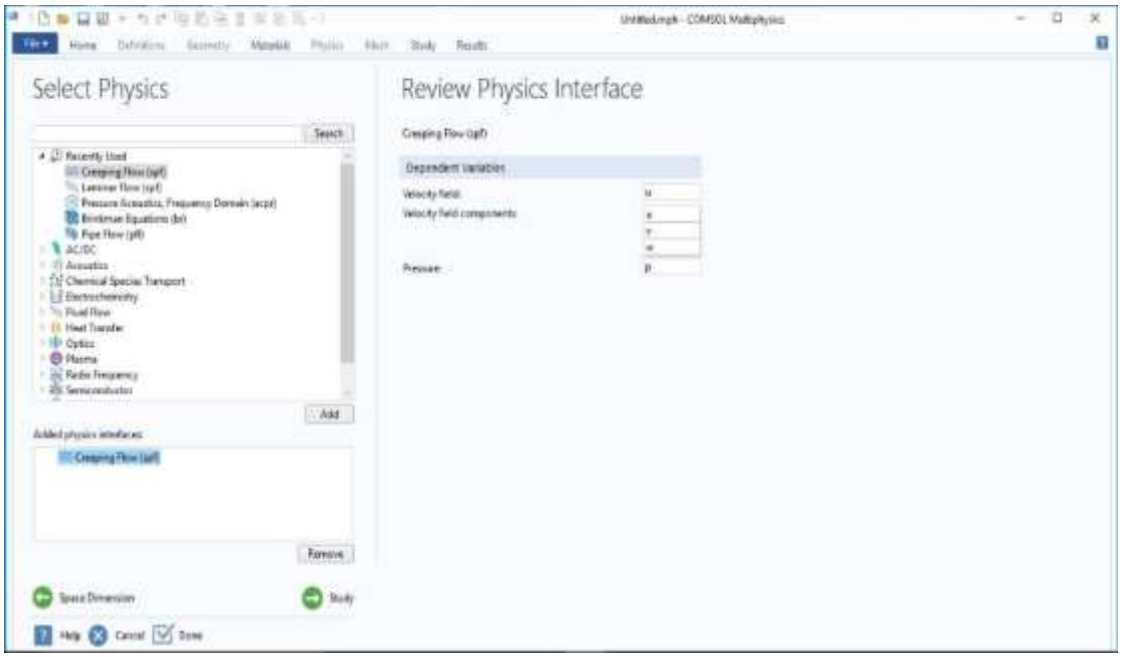

Figure 3.5: Selection of the physics interface (creeping flow).

4. Select the Study type that represents the solver or set of solvers that will be used for the computation. In the **Select study** tree, select **Preset Studies>Stationary** and click **Done**. The desktop is now displayed with the model tree configured according to the choices made in the Model Wizard in figure 3.6 blows.

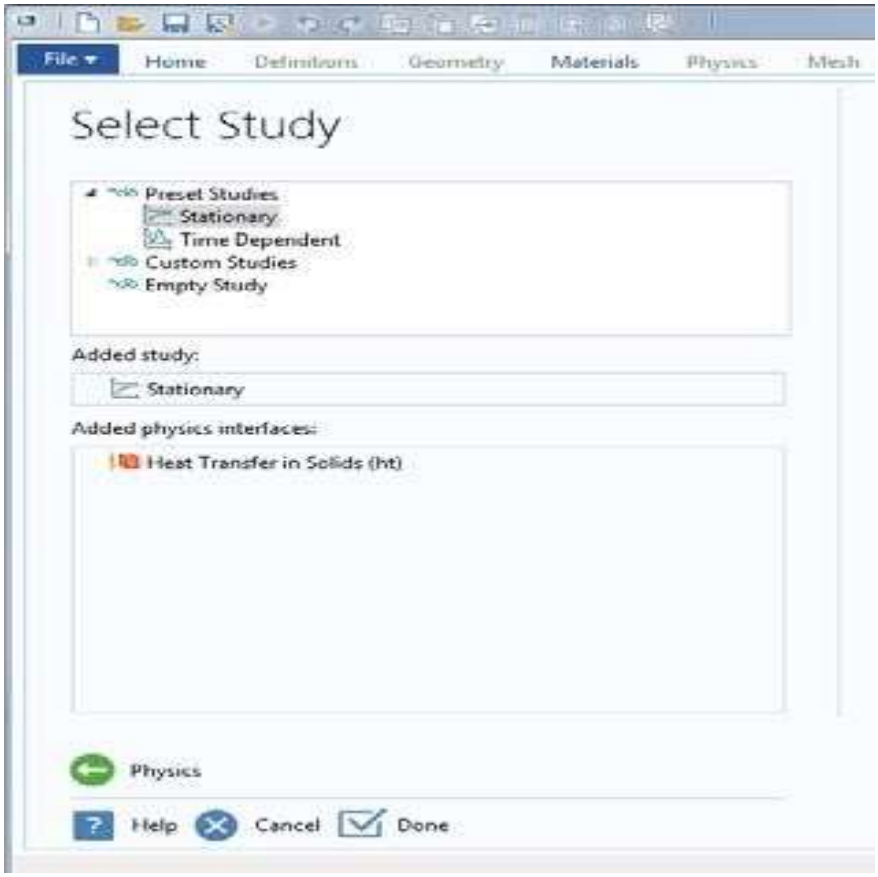

Figure 3.6: Study selection (stationary) of CFD

3.3.2 Geometry

There are three (3) steps to be taken under geometry;

1. Figure 3.7 presents the selection of units (From the **Length unit** list, choose **µm**)

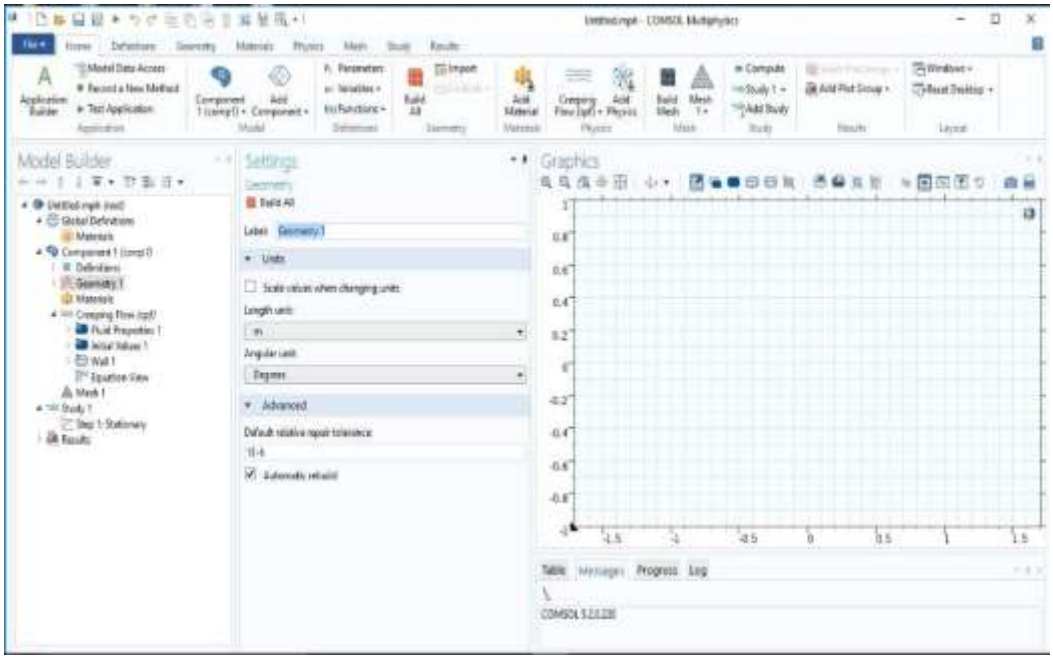

Figure 3.7: Model builder setting.

2. Import geometry (In the Model Builder window, under **Component 1**,right-click **Geometry 1** and select **Import)** to display the geometry in the Graphics window
3. Define parameters (In the **Model Builder**, right-click **Global Definitions** and choose **Parameters).** In the table, enter the name, expressions, values and description of parameters chosen shown in figure 3.8 blows.

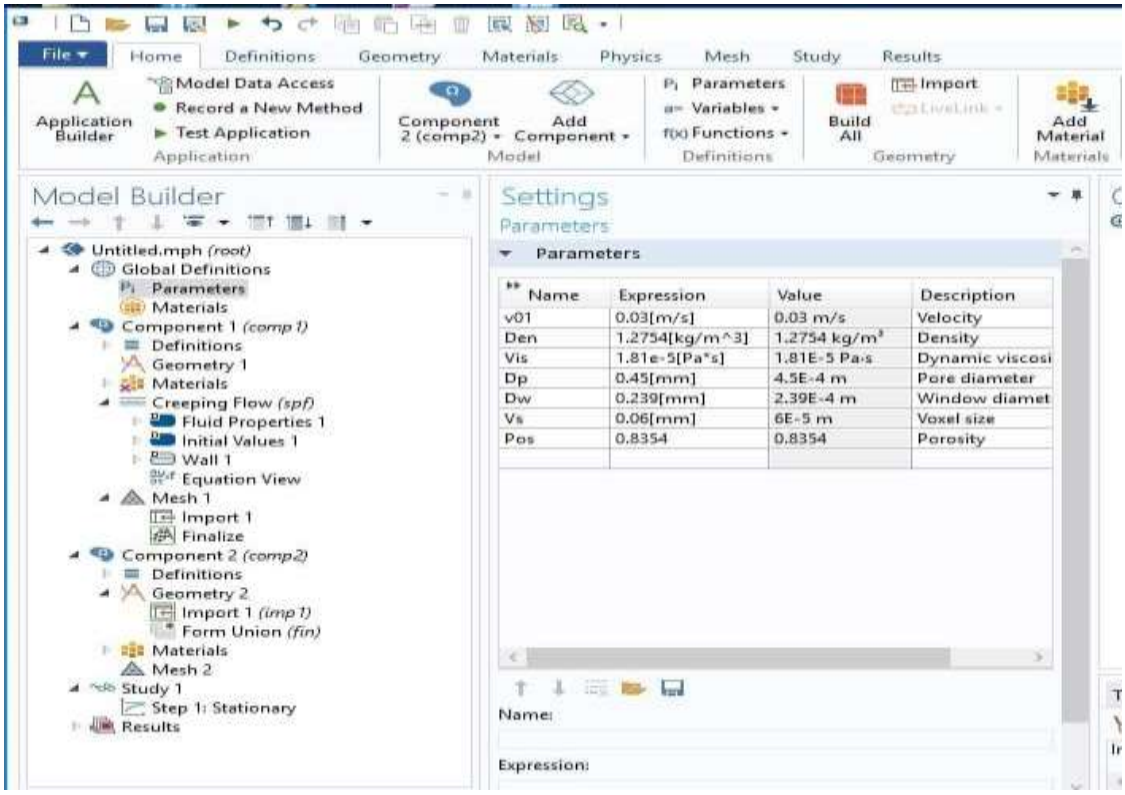

Figure 3.8: Parameters input of both the sample and material.

3.3.3 Materials

The materials node stores the material properties for all physics and all domains in a Component node. In the **Model Builder** window, under **Component 1 (comp1)** right-click **Materials** and choose **Blank Material**. Go to the **Settings** window for Material, locate the **Material Contents** section and enter the following settings in the Table 3.3. When entering the names corresponding to the ones in global definition, the others will appear.

Table 3.3: Properties of material (Air)

Property	Name	Value	Unit	Property group
Density	Den	Den0	kg/m³	Basic
Dynamic viscosity	Vis	Vis0	Pa·s	Basic

3.3.4 **Physics** (Comsol Multiphysics package)

Physics is a step in modeling process of Comsol Multiphysics version 5.2, software that involves the selection of flow equation and boundary conditions. With the geometry and materials defined, the next step is to select the boundary condition that is, specifying the inlet, outlet and symmetry of the imported geometry where air is the chosen material. A boundary condition is a form of an equation or a stated restriction that limits the possible solutions to a differential equation. It is a condition where a differential equation is solved. Setting out the right boundary condition when resolving the fluid models can help to differentiate between right and wrong or solve our computation easily. Selection of flow equation and appropriate boundary condition were chosen from the physics in the model builder of package. The flow equation was selected basically on the Reynolds number (N_{Re}); stokes equation was used to resolved flow in creeping flow ($N_{Re} < 1$) while neglecting inertial effect, at laminar flow Navier stokes equation was used ($1 < N_{Re} < 300$), finally Spalart Allmaras Reynolds Average Navier-Stokes (RANS) with (k-ε) model for resolving flow in turbulence ($N_{Re} > 300$) which was described in (Lage *et al.*, 2005). The boundary condition was assumed that:

1. The inlet: velocity was selected (v = 0 – 6.0m.s^{-1}), to specified constant velocity or a defined velocity. Pressure ($p = p_0$), use to describe fluid inlet perpendicular to the boundary
2. Outlet: Pressure ($p = p_0$), use to describe fluid outlet perpendicular to the boundary. (v = v_0), be careful not to over-specify.
3. No-slip on the solid walls of the structures (v = 0), zero velocity at the wall (Hesketh, 2008; Otaru, 2018).
4. Symmetry boundary along the symmetry planes and the velocity perpendicular to the plane of symmetry is zero similar to that of (Henry, 2007).

NB: The Navier-Stokes equation of flow in porous media is formed from the combination of the continuity equation and the momentum equation described below:

Continuity

$$0 = \nabla.(\rho v) \tag{3.1}$$

Creeping Flow

$$0 = \nabla.[PI + \mu(\nabla.v + (\nabla.v)^T) - \frac{2}{3}\mu(\nabla.v)I] + F \tag{3.2}$$

Navier-Stokes

$$\rho(v.\nabla)v = \nabla.[PI + \mu(\nabla.v + (\nabla.v)^T) - \frac{2}{3}\mu(\nabla.v)I] + F \tag{3.3}$$

Where μ is the dynamic viscosity of the fluid in kg/m.s; $v$is the velocity vector in m/s; ρ is fluid density in kg/m^3;p is the pressure measured in Pa.

Turbulent: Turbulent: The Spalart – Allmaras Reynolds Average Navier-Stokes with undamped turbulent kinetic viscosity (3x) its kinetic viscosity was solved for the single-phase steady state flow of fluid. This model is suitable for our velocity range of application, particularly, suitable for resolving both compressible and incompressible fluid flow with Mach number below 0.3. The non – application of wall function and flow on an entire flow field makes this model to converge faster with low memory utilization compared to other RANS models. Depending on the distance from the fluid to the closest wall, the Spalart-Allmaras model resolves the flow field down to the wall.

These are steps to be taken under physics (Comsol Multiphysics package);

1. On the **Physics** toolbar, click **Creeping flow** for stokes equation after finishing with creeping flow (N_{Re}>1), and in the setting window, locate physical model section.
2. On the **Physical model section** locate the neglect inertial term "unclick the **Box**" using Navier stokes equation for laminar flow (1<N_{Re}< 300).
3. On **Turbulence model** under physics settings, change **None** to **RANS** and locate the Turbulence model, select **Spalart Allmaras** model (N_{Re}> 300).
4. On the **Physics** toolbar, click **Boundaries** and choose **Inlet**, specify the desired inlet boundaries and in the **Settings** window for Inlet, locate the **Boundary Condition** section and choose **Pressure;** then locate the **Pressure Conditions** section and type p0 in the *p*0 text field.
5. On the **Physics** toolbar, click **Boundaries** and choose **Outlet** and select the desired outlet boundaries.

6. On the **Physics** toolbar, click **Boundaries** and choose **Symmetry** and select the symmetry Boundaries.

3.3.5 Mesh

The mesh settings determine the resolution of the finite element mesh used to discretize the model. The finite element method divides the model into small elements of geometrically simple shapes, in this case a linear tetrahedral mesh. However, since the geometry of the porous metal structures contains small edges and faces, a slightly finer mesh than the default setting suggests better resolving the variations of the stress field and giving a more accurate result. Refining the mesh size to improve computational accuracy always involves some sacrifice in speed and typically requires increased memory usage. In the **Model Builder** window, under **Component 1 (comp1)** right-click **Mesh 1** and choose **Build All** presented on figure 3.9.

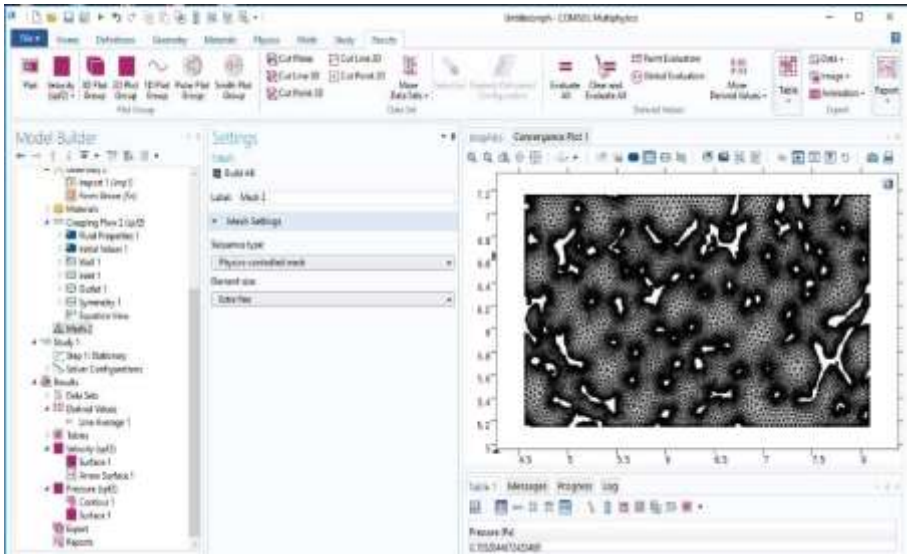

Figure 3.9: Mesh dependency study of CFD.

3.3.6 Study

In the beginning of setting up the model, a **Stationary** study was selected which implies that a stationary solver will be used to carry out the computation to generate convergence. On the **Home** toolbar, click **Compute.**

Figure 3.3 show the convergence plot of error against iteration number. The process has 7 iteration numbers, from the first iteration to the third iteration the error was 1 but as it progress to the fourth iteration, the error started reducing rapidly. Finally as it got to the seventh iteration (convergence point which is the last iteration) the error was approximately equal to zero.

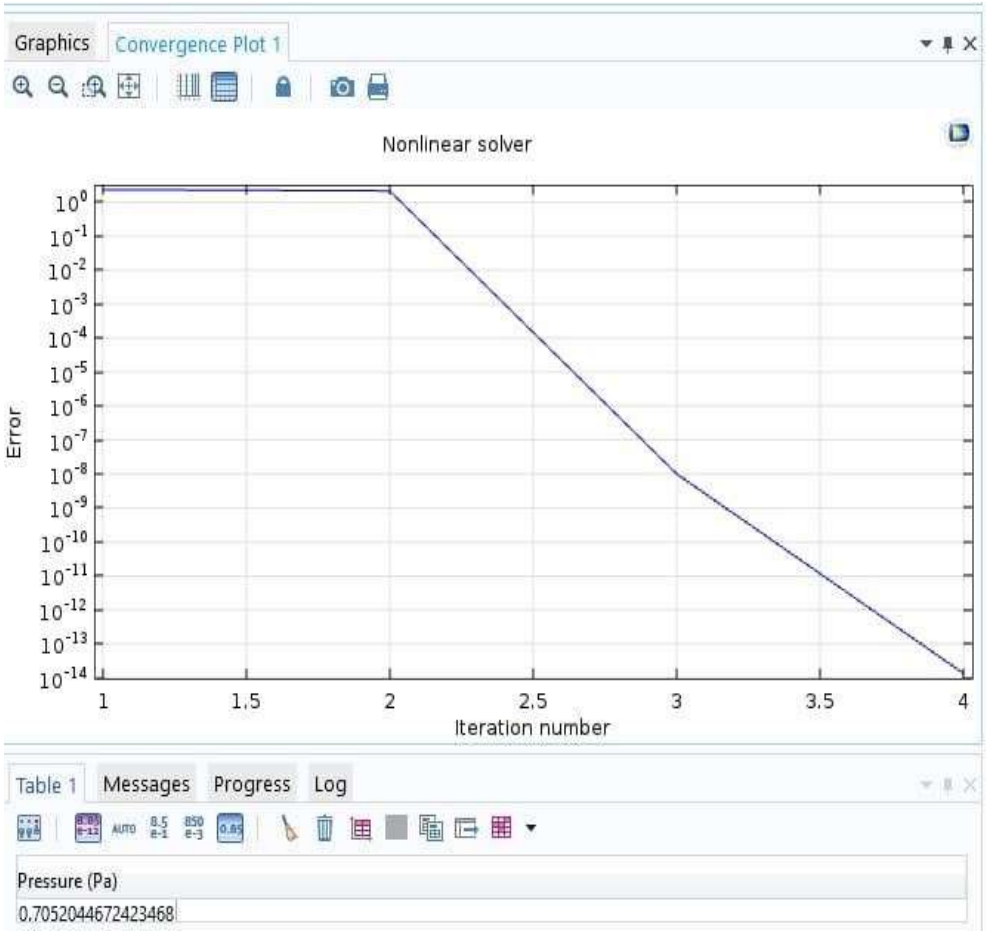

Figure 3.10: Convergence plot for error against number of iteration

3.3.7 **Result** (Comsol Multiphysics package)

Figure 3.11, present accurate plot on the velocity and pressure gradient is gotten on the step of CFD modeling and simulation of Comsol Multiphysics process.

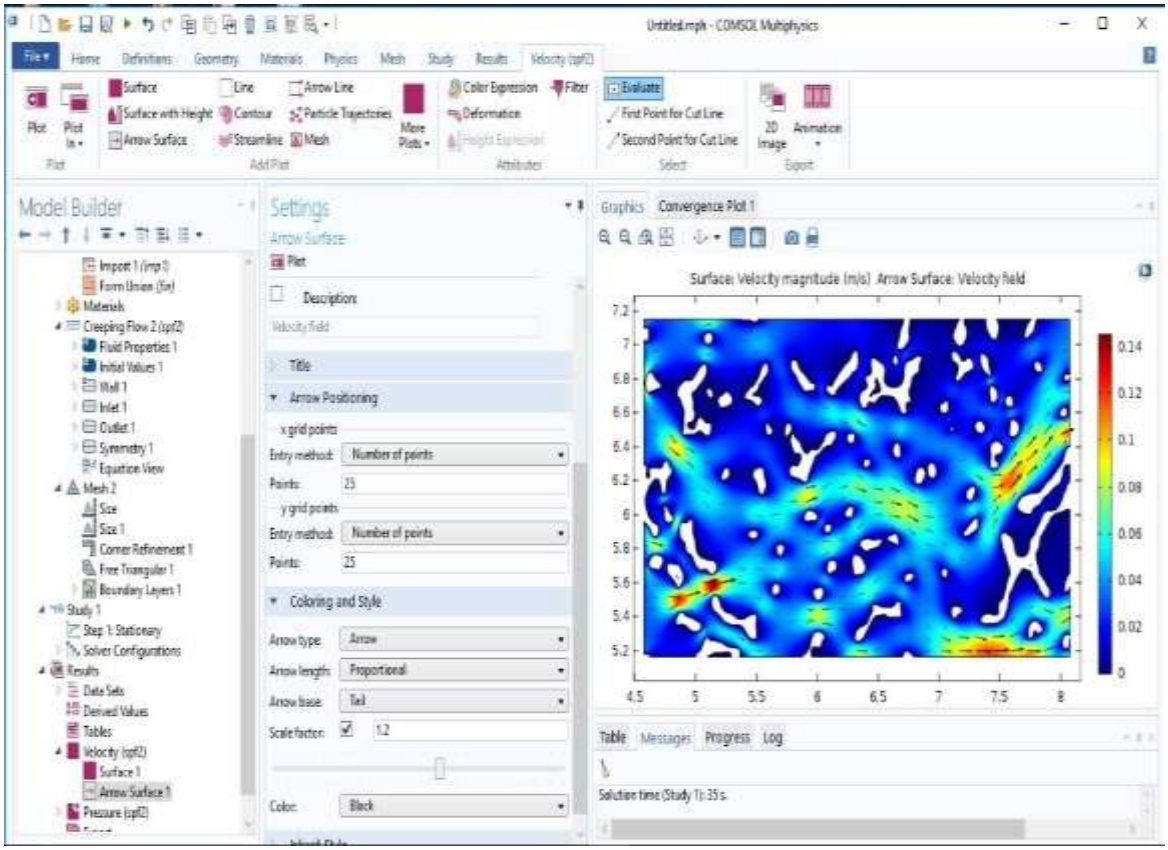

Figure 3.11: Velocity magnitude ($m.s^{-1}$) and arrow surface direction.

3.4 Investigation of Sudden Enlargement and Sudden Contraction on Hybrid/Stacked Porous Metals

Two highly porous metals with different pore sizes (Alantum 450µm (A) and Alantum 1200µm (B)) are stacked together (A + B) with the help of Synopsys-Simpleware™Software. Therefore, two types of hybrid/stacked samples were created which are differentiated by their geometrical thickness or length. The first hybrid/stacked sample is that of Alantum 450µm (2x) the length of Alantum 1200µm (2L A + 1L B). The

second hybrid/stacked sample were the both porous metals have equal length (1L A + 1L B). The modelling and simulation from (3.3) were carried out on each stacked sample to investigate the impact of sudden enlargement and sudden contraction. Below are the schematically steps;

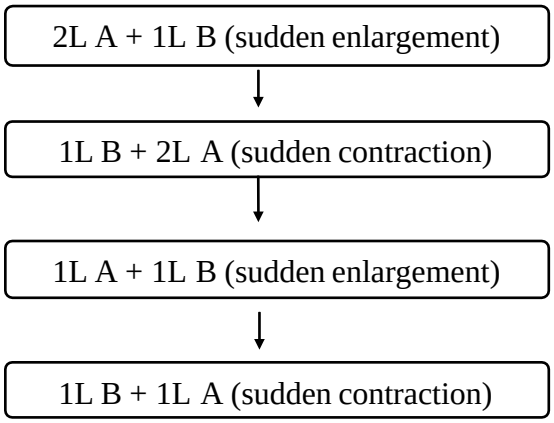

Figure 3.12: Sudden enlargement and sudden contraction steps for both stacked samples. (Where, 2L = 5.004mm, 1L (B) = 2.556mm and 1L (A) = 2.504mm.)

3.5 Determination of Permeability and Form Drag of all the Samples

Fluid flow with very slow velocity, characterised by pore diameter Reynolds number (N_{Re}) lees than one ($N_{Re}<1$), the acknowledged Darcy's law relates the fluid velocity and unit pressure drop developed across porous structures (Eqn 3.4). Fluid flow with high velocity, the Darcy-Dupuit-Forchheimer (Eqn 3.5) model relates the defined pressure drop per unit flow thickness (A_p) developed across porous materials as a function of the two most important parameters used to describe flow behaviour at very low (permeability, k_o) and high (Form drag coefficient, C) superficial fluid velocities (v_s), fluid dynamic viscosity (5)and fluid density (ρ).

$$\mathrm{A}p = \frac{y}{k_o} v_s \tag{3.4}$$

$$-\frac{6p}{6x_{\mathrm{i}}} = \mathrm{A}p = \frac{y}{k_o} v_s + \rho \mathrm{C} v_s^2 \text{ Oun and Kennedy, (2014)} \tag{3.5}$$

CHAPTER FOUR

4.0 RESULT AND DISCUSSION OF RESULTS

Presentation of the results obtained from chapter three and its discussion is made in this chapter using the data obtained from the CFD modelling and simulation of structural characterization of air flow through these commercially available high density porous metal samples; Alantum 450µm, Alantum 1200µm, Recemat 1723PPI, Recemat1116PPI, Porvair 7PPI and finally the hybrid/stacked samples of Alantum 450µm (A) plus Alantum 1200µm (B).

4.1 Results

Accurate and detailed information of the velocity and pressure gradients developed across the porous structures were achieved through meshing and mesh dependence study to quantify any likely trade-off between mesh count (mesh density) and computed values. Optimum mesh density ranging between 2.5 and 3.5MCells were utilized for a growth rate of 1.3, minimum edge length of 2.7 × voxel dimensions and maximum edge length of 6.5 × the minimum edge length for all the porous metal samples. Figure 4.1 present the mesh dependence study and from the study, optimum mesh structure was chosen based on the economical aspect like; power utility, time and system capacity. Figure 4.1 shows that both pressure ratios are almost equal to 100% for optimum mesh structure (3.5Mcell) and extremely mesh structure (6.5Mcell) with pressure ratio 99.0% and 99.5% respectively.

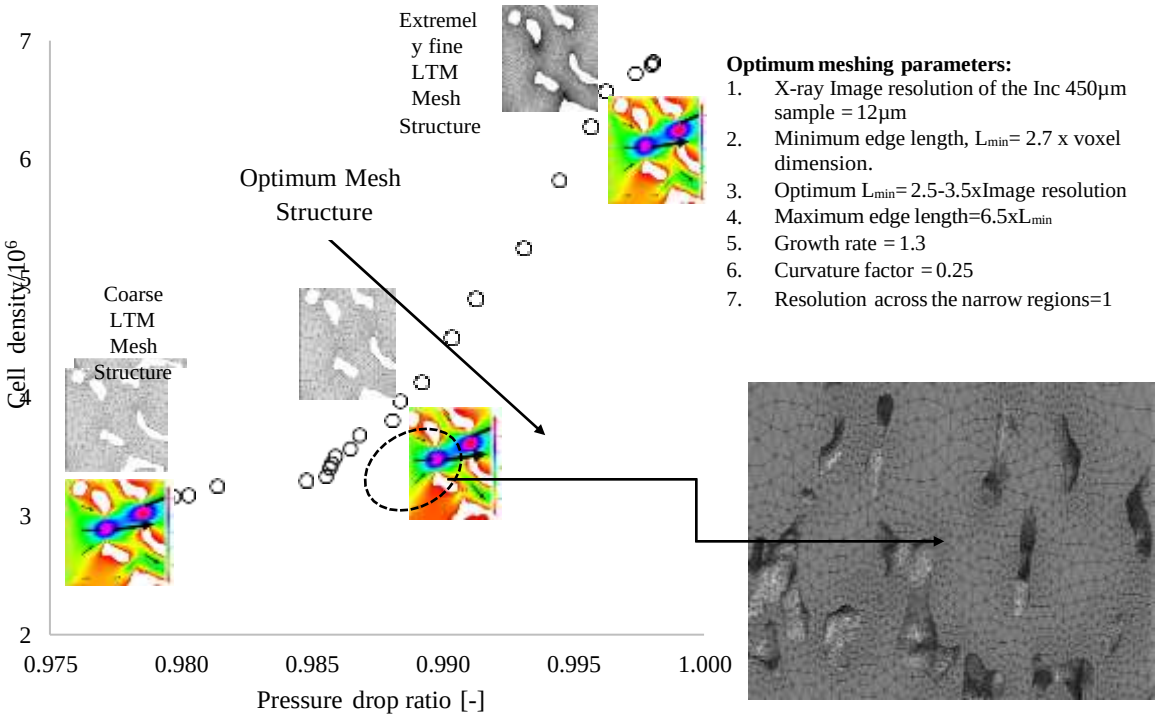

Figure 4.1: Linear tetrahedral mesh structures at the re-entrant edges (2.5-3.0MCells) and (d) is the plots of mesh density (cell count) against ratio of pressure drop obtained for different linear tetrahedral mesh (LTM) structures.

4.2 Discussion on Compressibility Effects

Figure 4.2 presents the 2D (left) and 3D (right) of the velocity (top) and pressure (bottom) streamline and arrow plots for the Porvair 7PPI foam structure indicating the flow of fluid from entrance to exit. The tendency of abridgement and the expansive morphological nature of the porous structures on the flowing fluid are indicated by the colour map in the legends (colour map indicate the increase on the number legend line, so as the number increases it shows an effect on colour differences). Evidently, the pore velocity (v_p) of the fluid at the "windows" of the porous matrices is somewhat higher than that at the fluid dominated pores and this often results, as seen, in a build-up of a high-pressure drop in these zones. Also, measurement of the average linear velocity or seepage velocity within the pore space (pore fluid velocity) was observably higher than the superficial fluid inlet velocity (v_s) thereby confirming the reliability and validation of Darcy expression similar to Whitaker (1986). This expression is valid for the continuity of fluid flow in porous

structures and relates the ratio of fluid superficial velocity to pore volume fraction as the seepage velocity of the flowing fluid.

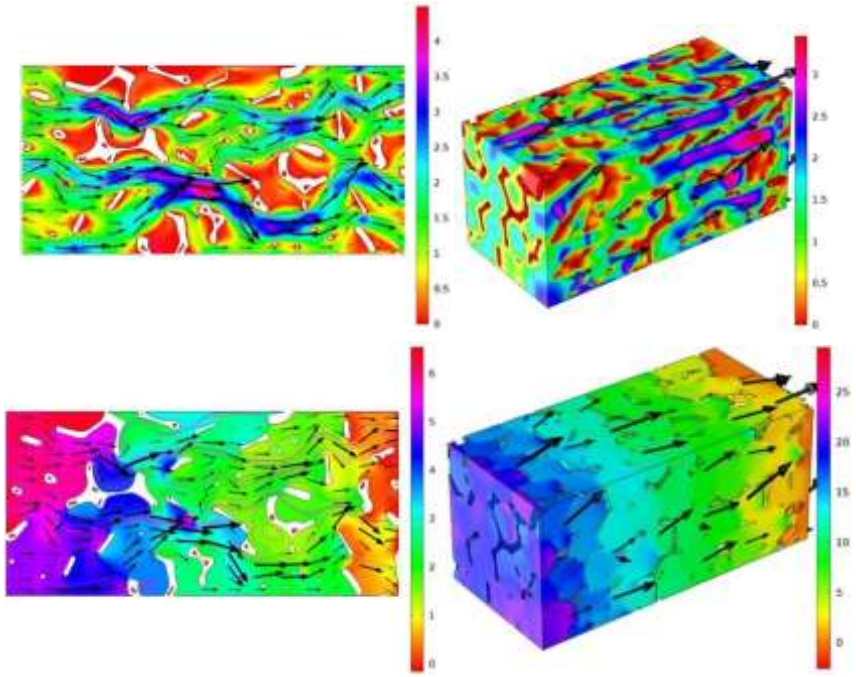

Figure 4.2: 2D (left) and 3D Velocity (top) and pressure (bottom) streamline plots of fluid flow across Porvair 7PPI Foam sample at Laminar superficial fluid flow velocity of 1.0m.s^{-1} (N_{Re} = 97).

Table 4.1 presents the macroscopic and flow parameters for the different porous metallic structures with key parameters like porosity, mean pore size, and mean openings or connectivity, mean ligament thickness, permeability, form drag coefficient and Forchheimer coefficient. The experimental analytical and computational model available in the literature has shown that the pressure drop developed across a porous body presented to a flowing fluid is a function of the superficial inlet fluid velocity of its thickness or length.

Table 4.1: A tabular representation of pore related parameter and flow information of all the samples including stacked samples.

								Darcy	Forchheimer-Turbulent	
µCT Sample	Symbols	Mean Pore Sizes, Dp (mm)	Mean Openings, Dw (mm)	Porosity (ε)	Mean Ligaments Thickness (mm)	Specific Surface, σ_{FB} (mm^{-1})	Specific Surface, σ_{FF} (mm^{-1})	$k_0/10^{-09}m^2$ Darcy	C (m^{-1})	C_F
Inconel 450µm	A	0.450	0.239	83.543	0.059	8.626	43.817	1.249	8541.546	0.342
Inconel 1200µm	B	1.230	0.489	90.621	0.176	3.216	31.095	15.562	1183.946	0.178
RCM-NCX 1723	D	1.855	0.691	80.962	0.254	3.010	12.800	16.888	1628.870	0.245
RCM-NCX 1116	C	2.454	1.286	89.809	0.341	1.519	13.281	65.359	594.663	0.181
Porvair 7PPI	E	1.466	0.858	89.690	0.405	2.254	19.602	25.143	1105.669	0.227
Inc. 450+1200µm (5.004+2.556mm)	2L A + 1LB	-	-	84.381	-	7.019	37.940	1.632	6919.980	0.318
Inc. 1200+450µm (2.556+5.004mm)	1LB + 2LA	-	-	84.381	-	7.019	37.940	1.752	6519.631	0.310
Inc. 450+1200µm (2.504+2.556mm)	1L A + 1LB	-	-	85.349	-	7.869	36.230	1.930	5583.382	0.277
Inc. 1200+450µm (2.556+2.504mm)	1LB + 1LA	-	-	85.349	-	7.869	36.230	2.097	5764.589	0.277

where Dp is the pore sizes, Dw is the pore connectivity, ε is the pore volume fraction, L_G is the ligament thickness, σ_{FB} is the ratio of the structure surface area to bulk volume, $\sigma_{FF}$is the ratio of the structure surface area to structure volume, k_0 is the permeability of the porous materials, C is the Form drag coefficient and C_F is the Forchheimer coefficient.

The unidirectional, steady state and fully developed pressure drop of airflow across these high density porous metals at different air superficial velocity typically between 1 x 10^{-6} to 1 x 10^{-2} m/s was used to determine the pressure drop per unit length presented in the Figure 4.3. The graphical plots for the porous structures presents the length-normalized pressure drop versus superficial air velocity relationship which shows a linear dependence fit or a close fit (R^2=1) indicating the measured pressure drops to be within the Darcy regime. It is observed from the figure 4.3 that the pressure-drop increases with increasing airflow velocity, that is, there is a close linearity between the pressure drop and the velocity (at very low velocity, the velocity is directly proportional to pressure drop), a result implying that inertial effects are negligible in line with (Dukhan and Patel, 2010) who mentioned that the relationship between pressure drop and velocity is linear when viscous stress dominates (Darcy regime) and the inertial forces are negligible. Hence, it could rightly be said that for a very low fluid velocity typified by N_{Re} below unity, the relationship between the fluid velocity and pressure gradient/drop is linear. Figure 4.4 shows the plot of unit pressure drop of airflow across all the samples against the superficial inlet velocity ranging from (0 – 6m.s^{-1}). Figure 4.5 presents the same plot to that of Figure 4.4 but excluding Inc. 450μm sample for clear understanding. Non linearity deviation between the fluid flow rate and pressure drop in figure 4.4 was observed for high fluid rate N_{Re} far above unity. These plots (figure 4.4) show a good curve fit of polynomial graph which indicate different regimes (Darcy – Laminar-Transition – Turbulent). It has confirmed the domination of inertial effect (Forchheimer expression) at a very high fluid flow reported in the literature.

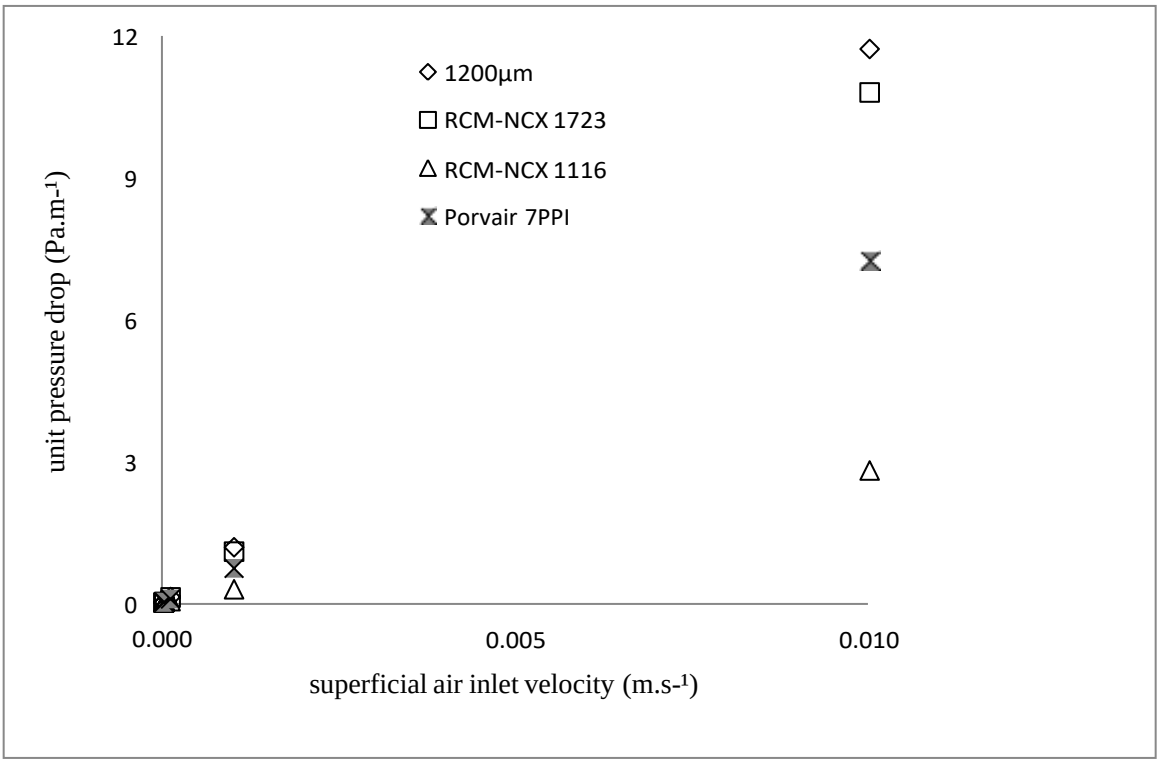

Figure 4.3: Plot of unit pressure drop (Pa) against superficial air inlet velocity (m/s) at Darcy regime of four structures excluding Inc. 450 µm.

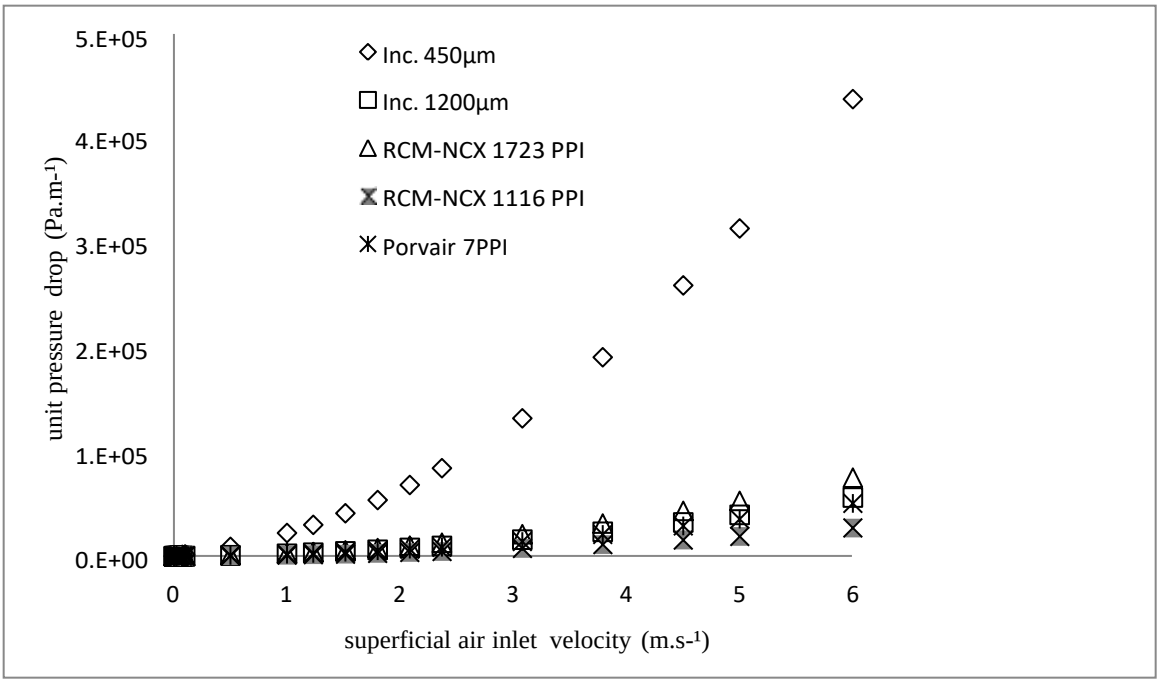

Figure 4.4: Plot of unit pressure drop (Pa) against superficial inlet velocity (m.s-1) of five porous structures (Darcy – Turbulent)

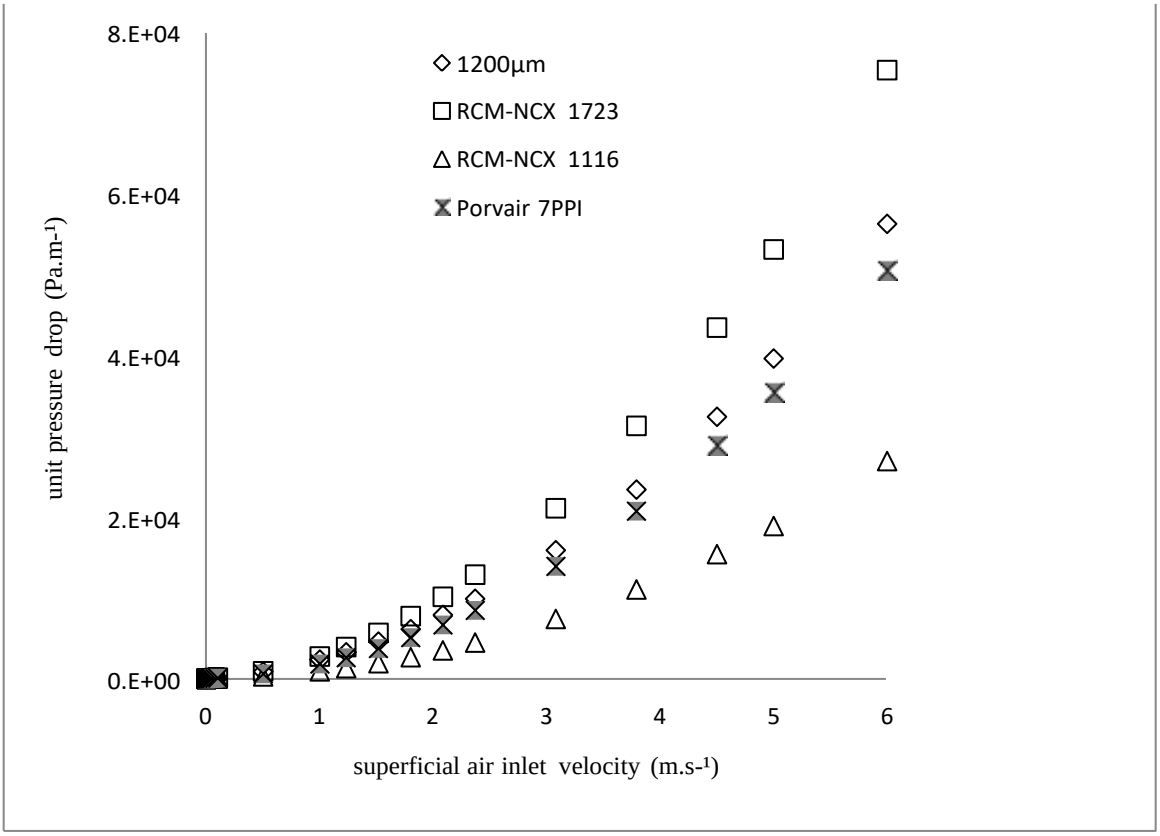

Figure 4.5: Plot of unit pressure drop (Pa) against superficial inlet velocity (m.s-¹) of four porous structures excluding (Inc. 450µm), (Darcy – Turbulent).

4.3 Effect of Sudden Enlargement and Contraction of Stacked Samples on Pressure Drop

An in-depth understanding of the effect of a sudden change in pore volume on the pressure drop of flowing fluid across these samples was made possible by stacking together samples with the lowest (Inc 450µm) and highest (Inc 1200µm) porosities as shown in Table 4.1. This enables an appreciation of the changes associated with a varying pore fluid volume for moving fluid in porous metals. Figure 4.6 (A, B, C, & D) present the streamline and arrow pressure plots indicating the direction of flowing fluid across the stacked samples. Figure 4.6A presents the changes in pressure gradient / drop for the moving fluid across the stacked samples for different porous sample thickness with inlet and exit effect. This behaviour can be likened to the pattern of fluid flow characterised by sudden enlargement and contraction in open conduits. The flow of fluid downstream the vicinity of the larger pores to smaller ones (contraction) causes an increase in pressure loss, resulting in a region

of separated flow which occurs at the contraction point. Figure 4.6B shows that the flow is severely disrupted as a result of the contour changes in the downstream flowing fluid within the pore walls. Conversely, the flow of fluid from smaller pores to larger ones can be described as sudden enlargement of the pore volume available for the flowing fluid. Observably, this results in the creation of an unstable pattern of flow eddies (reverse current largely dictated by high fluid velocity in the turbulent regime) at the expansion zone, and hence, a significant decrease in pressure drop within the porous material. The extent to which the pressure drop across the stacked samples lies within the two individually computed sample values was also determined by their porous layer thickness. That is, for a long enough Inc 450 µm sample (low pore sizes), twice that of the Inc 1200µm (A & B), developed pressure drop is evidently (Figure 4.7) closer to the unit pressure drop of the original Inc 450µm and this reduces significantly with reduced thickness taken from the sample (C & D). This is likely due to the increasing pore non-uniformity of the longer Inc 450µm in the stacked samples resulting in increasing tortuous path (Champoux and Stinson, 1992), hence, a higher-pressure drop for the flowing fluid.

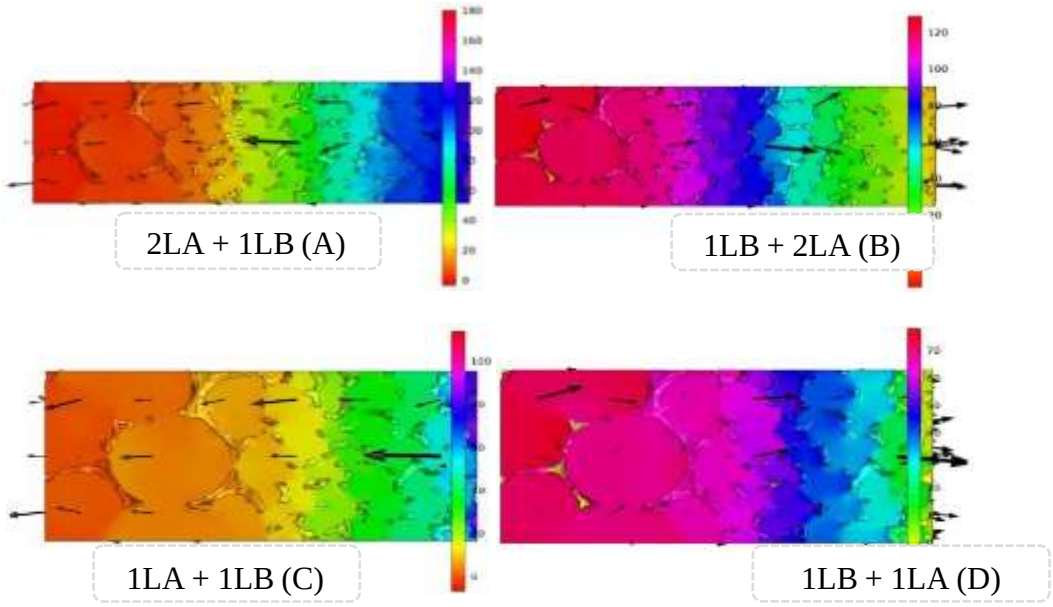

Figure 4.6: 2D streamline and arrow pressure plots direction of flowing fluid across the stacked samples. (A & B = Sudden enlargement and contraction of 2LA + 1LB respectively) and (C & D = Sudden enlargement and contraction of 1LA + 1LB respectively).

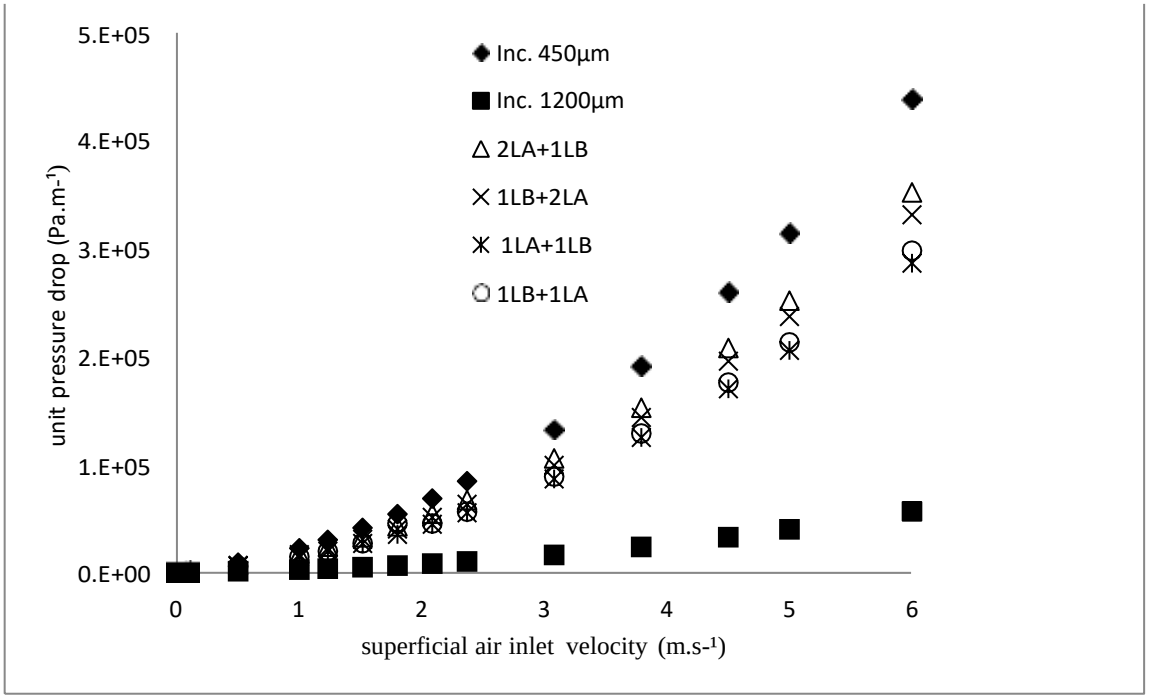

Figure 4.7: Plot of unit pressure drop (Pa) against superficial inlet velocity (m.s-¹) of real Inc. 450µm and 1200µm structure and sudden enlargement and contraction of stacked samples.

4.4 Effect of Structural Parameters and Flow Information on Pressure Drop

Higher values of pressure drops are observed for the samples with the lowest porosities and smallest windows while the lowest pressure drop was attained for the sample with largest openings/window size and conferred to have the highest porosity value. From Figure 4.4 it can be observed that the computed unit pressure drop developed is highest for the Alantum 450µm and lowest for the Recemat 1116 sample, the reason for this is that the samples are characterized by having the lowest (Alantum 450µm) and highest (Recemat 1116) mean pore sizes (*Dp*) and mean pore connectivity (*Dw*) as shown in Table 4.1.The larger the pore size the lower the pressure drop and the lower the pore size the larger the pressure drop similar to (De Carvalho *et al*, 2017). Taking into consideration Alantum 1200µm sample and Recemat 1723 sample, Figure 4.3 shows that the linear pressure gradient achieved for the Alantum1200µm is higher than that of the Recemat1723 and this can be attributed to

the reduced pore size of Alantum1200μm sample, hence, reduced permeability compared to the Recemat 1723 sample at low fluid velocity. This goes to show that pressure drop decreases with increasing pore size (increased permeability) and vice versa, that is, an increase or decrease in pressure drop is dependent on the pore size as shown in Figure 4.4 above. The variation in the pressure drop differences of these samples is associated with the porosity and openings between the connecting cell sizes within the microstructures. The size of the pores within the porous structure influences the tortuous path and interstices available for the flow of fluid (air) resulting in an increase or decrease in the pressure drop. Larger pore sizes (Recemat samples) as opposed to smaller pore sizes (Alantum samples) yielded a low tortuous path, low specific surface and large fluid volume which invariably resulted in low-pressure drops and high permeability of fluid measured across the foam structures. Figure 4.8 present the plot of normalised permeability against porosity of the real samples and Figure 4.9 present the plot of form drag against porosity of both the real and stacked sample. From Figure 4.8, it can be seen that as the porosity increases, so does the permeability increases, hence, permeability is dependent on porosity. A reduction in pore size results in a corresponding decrease in permeability which offers a greater resistance to flowing fluid which in turn brings about an increase in the pressure gradient across the samples. Therefore, the higher the permeability, the lower the pressure drop and vice versa.

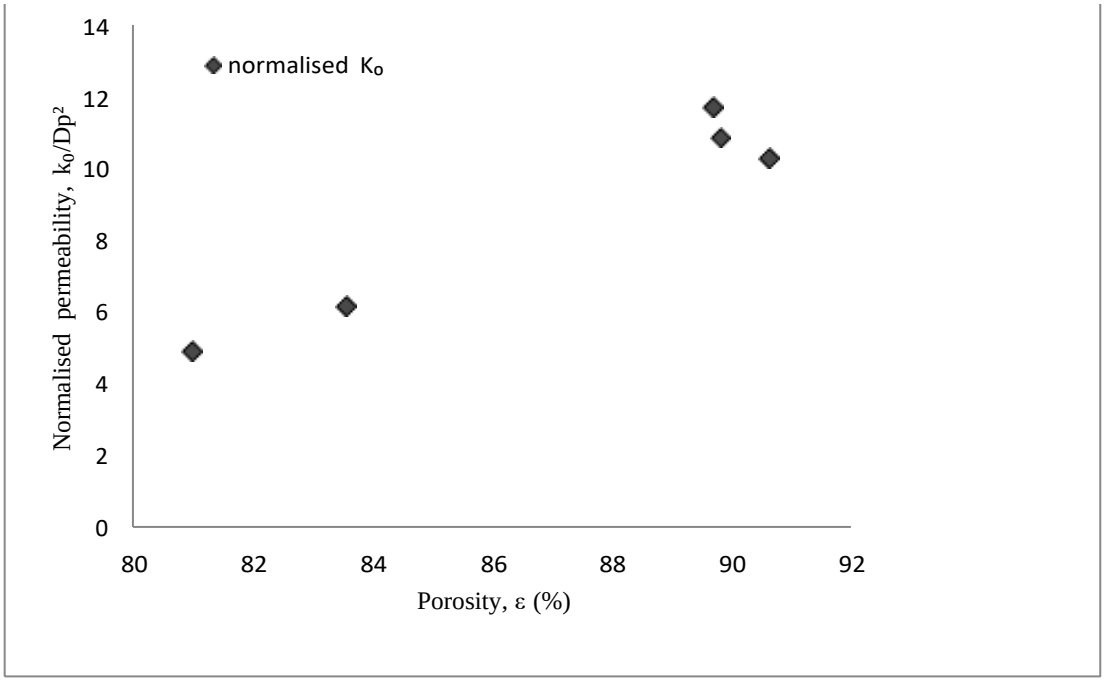

Figure 4.8: Plot of normalized permeability against porosity of real samples.

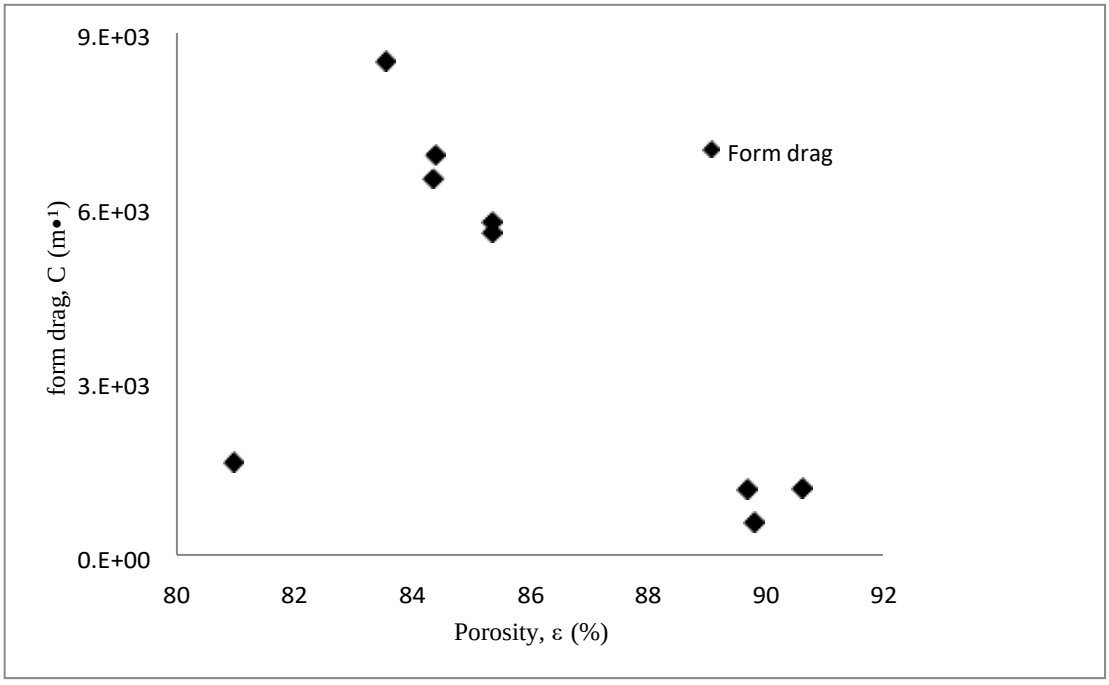

Figure 4.9: Plot of form drag against porosity of real and stacked samples.

4.5 Modelling Validation Accuracy

A validation of modelled accuracy were achieved by comparing the CFD modelled value (current) of unit pressure drop for the Inc. 450μm and Inc. 1200μm foam samples with experimentally measured data in (Otaru et al., 2019 and Otaru, 2018) of fluid flow across a 20mm thick sample of the real structures. From Figure 4.10, comparing the CFD modelling to experimentally measured value data shows a good accurate validation agreement within reasonable scatter for experimentally measured porosity (ε) 0.839 (Inc. 450μm) and 0.900 (Inc. 1200μm) and superficial air inlet velocity ranging between 0.5 and 4.5ms^{-1}. Observably from Table 4.2, the measured values of permeability and Form drag coefficient for the 20mm thick Inc 450μm sample are 1.69 ± 0.03 x 10^{-09} m^2 and 8566.4 ± 150 m^{-1} respectively. The CFD computed values of the permeability and Form drag coefficient for this range of superficial fluid velocities are 1.60 x 10^{-09} m^2 and 8530.8m^{-1}respectively, showing excellent agreement between measured and simulated values. Generally, the samples shows a little discrepancy for permeability and form drag from Table 4.2, and these was due to structural parameters and thickness effect of the experimentally measured like porosity (89%) and pore size (1.249mm) in (De Carvalho *et al*, 2017) to the current CFD modelled value porosity (81%) and pore size (1.855mm).

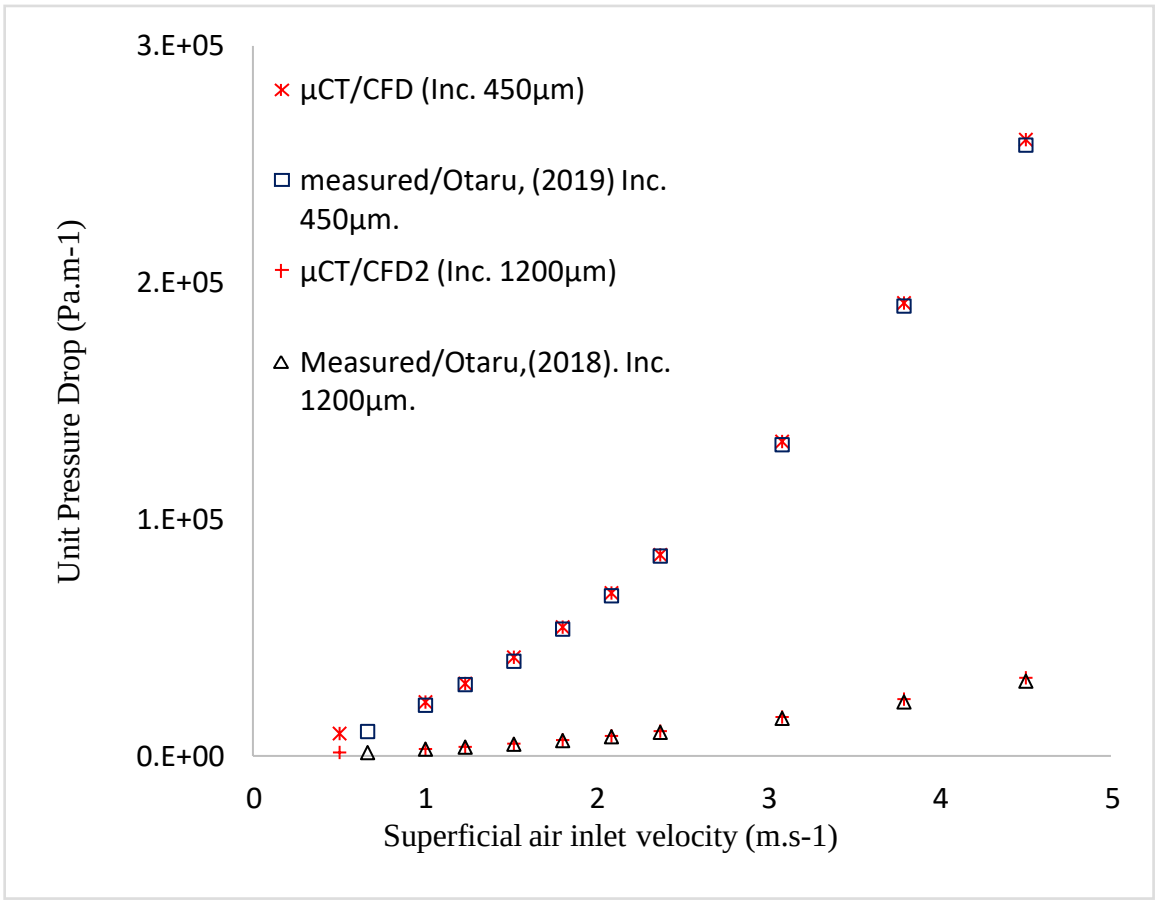

Figure 4.10: Plots of measured (literature) and CFD modelled [Current] unit pressure drop against superficial air inlet velocity for Inc. 450 µm and Inc. 1200µm porous metallic structure

Table 4.2: Comparison of K & C values (current) to some published in literature.

Samples	ε (%)	K x 10^{-9} (m^2)	C (m^{-1})	References
Inc. 450 µm	0.835	1.60	8541.55	Present
Inc. 450 µm	0.839	1.69	8566.40	Otaru et al. (2019)
Inc. 450 µm	0.84	1.43	-	Oun and Kennedy (2014)
RCX 1116 PPI	0.898	92.62	594.66	Present
RCX 1116 PPI	0.92	104	-	Kim et al. (2000)
RCX 1723 PPI	0.809	16.89	1628.87	Present
RCX 1723 PPI	0.887	11.18	662	De Carvalho et al. (2017)
Inc. 450 + 1200µm	0.853	1.93	5583.38	Present
Inc. 580 + 1200µm	0.852	3.17	2314	De Carvalho et al. (2017)

CHAPTER FIVE

5.0 CONCLUSION AND RECOMMENDATIONS

5.1 Conclusion

Computational Fluid Dynamics CFD investigation of pressure drop across highly porous metallic structure has been resolved via tomography datasets for superficial velocity ranging from ($0 – 6m.s^{-1}$). This work provides an insight understanding into the determination of pressure drop and the flow information of the porous samples from Darcy – Turbulent flow regime.

The combined modelling approach of 3D advanced imaging techniques and computational fluid dynamic modelling and simulation enabled an in-depth understanding of the changes in pressure gradient / drop resulting from the sudden change in pore volume and sizes and entrance and exit effects. Numerically, the pressure drop at superficial inlet velocity at $1m.s^{-1}$ of Inc. 450μm with smaller pore size and Recemat 1116PPI with lager pore size are 112.48pa and 12.33pa respectively.

Measuring and controlling the unit pressure drop developed across these high-density porous structures (stacked samples) are imperative to the design of porous metallic structures with enhanced performance. The knowledge of sudden enlargement and sudden contraction of these structures is important in the field of fluid mechanics.

From the present work it also proven that all types of open cell porous metal like pack bed, adapted porous metal, bottleneck and highly density porous metal

including stacked samples obeys and confirmed Darcy expression (viscous dominated were inertial effect are neglected) and Forchheimer expression that shows the presence of inertial effect (form drag).

The effects of the variation of geometrical parameters like porosity and pore size were investigated. It was shown that a pore size reduction determines an increase of the pressure drop/gradient across the samples. The effect of variation in the porosity was also considered showing that the dependence of the permeability on the porosity.

Supportable agreements between CFD modelled data against empirical measurements available in the literature were substantiated.

5.2 Recommendations

This current work enables more research gap for further knowledge which may include the following;

Numerical modelling and simulation of reverberation cat-back in automobile muffler via integrated pack beds and porous metallic structures.

CFD simulation of flow and heat transfer in stacked porous metal structure.

5.3 Contribution to Knowledge

This research shall contribute the following into resolving pressure drop across high density porous metallic structure of single and stacked samples;

The work accurately represents the pressure drop developed for a moving fluid across commercially available high density porous metallic structures working from X-ray

computed tomography datasets. The modeling approach quantifies the combined effects of pore volume fraction (80 – 95%) and pore size (0.2 – 5.0 mm).

The combination of advanced imaging technique and computational fluid dynamics modeling and simulation used herein provide an in-depth understanding of flow information of single or stacked samples of microcellular metallic foam that would have been difficult to handle experimentally. Numerically, the pressure drop at velocity 1 $m.s^{-1}$ of Inc. 450 µm and 1200 µm samples are 112.48 pa and 14.52 pa respectively and after stacking of the both samples the pressure drop at that same velocity become 72.57 pa.

REFERENCES

Abdulnaser S (2009): Computational fluid dynamics, *Abdulnaser Sayma and ventus publishing APS*, ISBN-978-87-7681-430-4. pp 13-50.

Ahmed N.M.A, Nasser A & Nabeel N.J.A, (2018): High-Porosity metal foams: potentials, applications, and formulations. *IntechOpen*. 8: pp 182-200

Ashby, M. F. & Tianjin, L. U. (2003): Metal Foams: A Survey, *Science in China Series* (b), **46**, No. 6, pp 521-530.

Ashby, M. F., Evans, T., Fleck, N. A., Hutchinson, J. W., Wadley, H. N. G. & Gibson, L. J. (2000): Metal Foams: *A Design Guild (1st edit)*. Oxford, UK: Butter- worth-Heinemann.

Azzopardi, B. J (2011): Enlargement Flow and Pressure Change in Pipe. *THERMOPEDIA*^{TM}, DOI;10.1615/Atoz.e.enlargement-flow.

Baloyo J. M, (2016): Open-cell porous metals for thermal management applications: fluid flow and heat transfer, *Materials Science and Technology*. 33(3), pp 265-275

Banhart, J. (2014): Manufacturing Routes for Metallic Foams. *JOM*, 52(12): pp 22-27.

Banhart J., M. Ashby & N. Fleck: (1999): Metal foams and porous metal structures, Breman, Germany, MIT. pp 1-2

Blick E. F. & F. Civan: (2013): Porous-media momentum equation for highly accelerated flow, *SPE Reserv. Eng*., 3, (3): pp 1048–1052.

Bram M., C. Stiller, H. P. Buchkremer, D. Stöver& H. Baur: (2000): High-porosity titanium, stainless steel, and superalloy parts, *Adv. Eng. Mater*., 2, (4): pp 196–199

CADENCE PCB SOLUTION (2020): finite element method vs. finite volume method in field solvers for electronics; PCB Design and analysis.

Champoux Y & Stinson MR, (1992): On acoustical models for sound propagation in rigid frame porous materials and the influence of shape factors. *J Acoustic Soc Am*, 92(2): pp 11, 20–31.

Choe H. D. D., (2004): Mechanical properties of oxidation-resistant Ni–Cr foams. *Materials Science and Engineering A*, 2004. 384(1-2): pp 184-193.

Cornell D & Katz D. L (1953): 'Flow of gases through consolidated porous media', *Ind. Eng. Chem*., 45, (10): pp 2145–2152.

DellaTorre A., G. Montenegro, G.R. Tabor & M.L. Wear, (2014): CFD characterisation of flow regimes inside open foam substrates. *Int. Journal of Heat and Fluid Flow*. 50: pp 72-82

Despois, J. F, & A. Mortensen, (2005): Permeability of open-pore microcellular materials. *Acta Materialia*, 2005. 53(5): pp 1381-1388.

De Carvalho T. P, Morvan H. P & Hargreaves D, Oun. H and Kennedy A (2017): Pore-scale Numerical Investigation of Pressure Drop Behaviour across Open-Cell Metal Foams. *Tran Porous Med*. 117(2): pp 311-336

De Lemos, M. J (2012): Turbulence in Porous Media: Modeling and Applications. *Elsevier, Amsterdam.* (2^{nd} edition): pp 1-350.

Dixit, U. S, (2014): Finite element method, An introduction: Dept. of Mechanical Engineering India Institute of Technology Guwahati,-781 39.

Dmitri K &Jari H (2014): Finite element method for Computational Fluid Dynamic; *A practical Guide*. 57(4): pp 642

Dukhan, N. & Patel, K. (2010): Entrance and exit effects for fluid flow in metal foam. In: *AIP Conference Proceedings, vol*. 1254, pp 299–304.

Dukhan, N. (2006): Correlations for the pressure drop for flow through metal foam. *Exp. Fluids*. **41**: pp 665–672

Dukhan, N. & Ali, M. (2012): Effect of confining wall on properties of gas flow through metal foam: an experimental study. *Transp. Porous Med*. **91**, pp 225–237.

Dukhan N, (2013): Metal foams: fundamental and applications. USA: DESTECH Publication, *Inc. Technology & Engineering*; pp 1–310.

Du Plessis, J. P. &Masliyah, J. H. (1988): Pressure-drop prediction for flow through high porosity metallic foams. *Transp. Porous Media*, 3, pp 145-161.

Erik D, (2009): Introduction to finite element method in Computational Fluid Dynamic.; *Researchgate*: CFD. pp 235-274

Farkas T., G. Zhong & G. Guiochon: (1999): Validity of Darcy's law at low flow-rates in liquid chromatography, *J. Chromatogr*. A, 849, (1): pp 35-43.

Forchheimer, P. (1901): WasserbewegungDurch Boden. *Zeitschrift Ver. Deutsch Ing.*, vol. 45, pp 1782–1788.

Fujibayashi M., M. Neo, H. M. Kim, T. Kokubo& T. Nakamura, (2004): Osteoinduction of porous bioactive titanium metal, *Biomaterials*, 25, (3): pp 443–450.

Furman E. L, Finkelstein A. B, &Cherny M. L. (2013): The permeability of aluminium foams
produced by replicated-casting. *Metals*; 3: pp 49–57.

Gladysz G. M. & K. K. Chawla (2015): Voids in materials: from unavoidable defects to designed cellular materials, Amsterdam, *Elsevier*. 40: pp 1-214.

Hassanizadeh, M. & Gray, W. G. (1987): Toward an Improved Description of the Physics of
Two-Phase Flow. *Advances in Water Resources*, vol. 16, no. 1: pp 53–67.

Henry, D. L. H, (2007): Experimental analysis and macroscopic and pore- level flow simulation to compare non-Darcy flow models in porous media, PhD Thesis. Colorado School of Mines, US. pp 211-230.

Hesketh, R. P. (2008): Flow between Parallel Plates-Modified from the COMSOL ChE Library
Module, Department of Chemical Engineering, Rowan University, pp 3-4.

Jorges P. A, & Malcom J. C. (2010): Recent-trends in porous sound-absorbing materials. *Sound Vib*; 44: pp 12–7.

Khayargoli, P., Loya, V., Lefebvre, L. P., &Medraj, M. (2004): The impact of microstructure on the permeability of metal foams. Proceedings of the CSME, London. pp 220-228.

Kim S. Y., Paek J. W & Kang B. H. (2000): Flow and heat transfer correlations
for porous fin in a plate-fin heat exchanger, *J. Heat Trans.*, 122, (3): pp 572–578.

Kececioglu I & Jiang Y. (1994): Flow through Porous Media of Packed Spheres Saturated with Water. *ASME J. Fluids Eng*; 116: pp 164-170

Kennedy A, (2012): In Porous metals and metal foams made from powders. Powder Metallurgy, KatsuyoshiKondoh, *Intech Open*; 2: pp 31-48.

Kouidri A. &Madani, B., (2016): On the effective thermal conductivity of a three-dimensionally structured fluid-saturated metal foam. *Mechanics of Materials*, 99: pp 79-87.

Lage J. L, Krueger P. S &Narasimham A (2005): Protocol for Measuring Permeability and Form Coefficient of Porous Media. *Physics of Fluids*, 17: pp 88-101.

Lee, Y. H., Choi, J. E., & Kang, K. J. (2006): A new periodic cellular metal with kagome trusses and its performance. Paper at the ASME Conference Proceedings. *(ASME International Mechanical Engineering Congress and Exposition)*, Chicago, USA. 15467: pp 629-635

Lee, J., Sung, N., Cho, G. & Oh, K. (2010): Performance of radial-type metal foam diesel particulate filters. *Int. J. Automot. Technol*. **11**(3): pp 307–316.

Lu. T. J. F & Chen H, D. (2014): Sound Absorption of Cellular Metals with Semi-Open Cells, *J. Acoust. Soc. Am.* 108 (4): pp 1697-1708.

Maire, E., Colombo, P., Adrien, J., Babout, L. &Biasetto, L. (2007): Characterization of the morphology of cellular ceramics by 3D image processing of X-ray tomography. *J. Eur. Ceram.* Soc. **27**(4): pp 1973–1981

McNeil, D. A, & Morris, S. D., (1995): A Mechanistic Investigation of Laminar Flow through an Abrupt Enlargement and Nozzle and its Application to Other Pipe Fittings. *Report EUR* 16348EN.

Medraj, M., Baril, E., Loya, V. & Lefebvre, L.P.; (2007): The effect of microstructure on the permeability of metallic foams, *J. Mater. Sci*. **42**(12): pp 4372–4383.

Otaru A. J, Morvan H. P & Kennedy A. R, (2018a): Measurement and Simulation of Pressure Drop across Replicated Microcellular Aluminium in the Darcy-Forchheimer Regime. *Acta Materialia*. 49: pp 265-273.

Otaru A. J, Morvan H. P & Kennedy A. R (2018b): Modelling and Optimisation of Sound Absorption in Replicated Microcellular Metals. *ScriptaMaterialia*. 150: pp 152-155.

Otaru A. J, (2018): Fluid flow and acoustic absorption in porous metallic structures using numerical simulation and experimentation, PhD Thesis. United Kingdom: The University of Nottingham.

Otaru A. J (2019): Enhancing the sound absorption performance of porous metals using tomography images Appl. *Acoust.*143: pp 183–9

Otaru, A. J., Morvan, H. P. & Kennedy, A. R., (2019): Airflow Measurement across Negatively Infiltration Processed Porous Aluminium Structures, *AIChE Journal*. 65: pp 13, 55-64.

Otsu, N. (1975): A threshold selection method from gray-level histograms. *Automatica.***11**(285–296): pp 23–27

Oun H & Kennedy A. R (2014): Experimental investigation of pressure drop characterization across multilayer porous metal Structure, *J. Porous Mater*21: pp 11, 33–41

Piller M., D. Casagrande, G. Schena, & M. Santini (2014): Pore-scale simulation of laminar flow through porous media**,** *Journal of Physics*: Conference Series **501;** doi:10.1088/1742-6596/501/1/012010

Pedras, M. H. & De Lemos, M. J (2001): Macroscopic turbulence modeling for incompressible flow through undeformable porous media. *Int. J. Heat Mass Transf.* **44**(6): pp 1081–1093

Petrasch, J.,Wyss, P., Stämpfli, R. & Steinfeld, A. (2008): Tomography-based multiscale analyses of the 3D geometrical morphology of reticulated porous ceramics. *J. Am. Ceram*. Soc. **91**(8): pp 2659–2665

Ranut P, Nobile E & Mancini L, (2014): High- Resolution Microtomography-Based CFD Simulation of Flow and Heat Transfer in Aluminium Metal Foams. *J.applthermaleng*. 69(1): pp 230-240.

Sharafat S., N. Ghoniem, M. Sawan, A. Ying & B. Williams: (2006): Breeder foam: an innovative low porosity solid breeder material, *Fusion Eng. Des*., 81, (1–7): pp 455–460.

Simpleware Ltd Reference Guide (2014): Converting 3D images into models Version 7.0

Sheppard, A. P., Sok, R. M. &Averdunk, H (2004): Techniques for image enhancement and segmentation of tomographic images of porous materials. *Phys. A: Stat. Mech. Appl*. **339**(1): pp 145–151.

Sun Z., X. Tang & G. Cheng: (2013): Numerical simulation for tortuosity of porous media, Micro. *Meso. Mater*, 173: pp 37–42.

Thauvin F & Mohanty K. K. (1998): Network modelling of non-Darcy flow through porous media, *Transp. Porous. Med*., 31, (1): pp 19–37.

Veruscha, P. (2004): Viscous Flow Through Sudden Contraction; Dissertation Submitted in Fulfillments of the Degree of Doctor Technologiae in the Faculty of Engineering Cape Technikon, Cape Town, South Africa

Whitaker, S, (1986): Flow in Porous Media 1: a Theoretical Derivation of Darcy's Law. *Transport in Porous Media*, vol. 1: pp 3–25.

White F.: (2009): Fluid mechanics, 7th edn. New York, McGraw-Hill.

Xiao Z (2013): Heat Transfer, Fluid Transport and Mechanical Properties of Porous Copper Manufactured by Lost Carbonate Sintering, AThesis submitted in accordance with the requirements of the University of Liverpool for the Degree of Doctor in Philosophy.

Yang X, Bai J & Lu T. (2008): A simplistic analytical model of permeability for open-cell metallic foams. *Chinese Journal of Theoretical and Applied Mechanics*; 46: pp 682-686.

Yashar S. V (2015): Numerical Investigation of Parameters Impacting the Wall Thickness Carbon Nanotubes Manufactured by Template-Based Chemical Vapour Deposition. A Thesis Submitted In Partial Fulfilment of the Requirement for the Degree of Master of Science in Mechanical Engineering at Rochester Institute of Technology, New York. pp 17-77

Zhao Y. Y, Fung T., Zhang L. P. & Zhang F. L. (2005): Lost carbonate sintering process for manufacturing metal foams. *ScriptaMaterialia*, 52(4): pp 295-298.

Zhou, J. (2006): Porous Metallic Materials, *Advanced Structural Materials*, 1st edn. Winston O.
Soboyejo, CRC Press, *Taylor & Francis Group,* USA, pp 1-22.

Zou, C., Zhang, E., Li, M., & Zeng, S. (2008): Preparation, microstructure and mechanical properties of porous titanium sintered by Ti fibres. *Journal of Materials Science*: Materials in Medicine, 19(1): pp 401.

Zuo W (2005): Introduction to Computational Fluids, *FAU Erlangen-Nurnber.* pp 3-8.

Zhao C. Y. (2012): Review on thermal transport in high porosity cellular metal foams with open cells. *Int J Heat Mass Transfer*, 55: pp 3618-3632.

Zhong W, X. Li, F. Liu, G. Tao, B. Lu & T. Kagawa, (2014): Measurement and correlation of pressure drop characteristics for air flow through sintered metal porous media, *Transp. Porous. Med*., 101, (1): pp 53–67.

Zhou P, (1993): Finite Different Method, In Numerical Analysis of Electromagnetic Field, Electric Energy System and Engineering Series. *Springer, Berlin, Heidelberg*. (1st edn) Doi.org/10.1007/978-3-642-50319-1_3.

APPENDICES

Appendix A: Velocity and Pressure Streamline Plots of Flow across Inconel (Alantum 450µm)

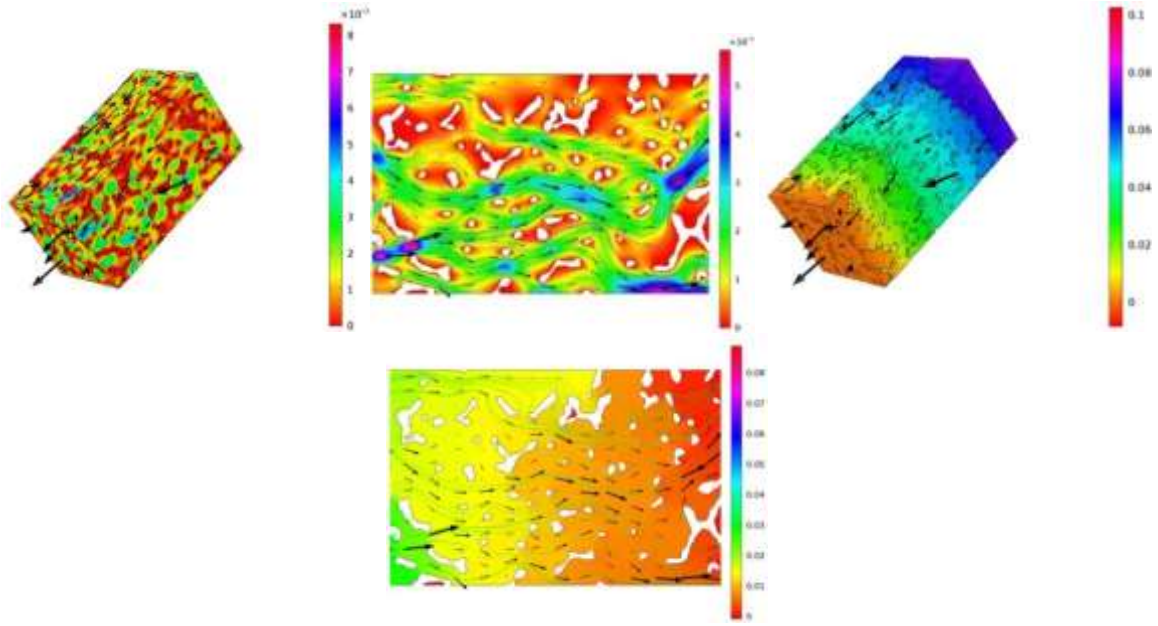

Appendix A1: 3D and 2D Velocity ($m.s^{-1}$) and pressure (Pa) streamline plots of fluid flow across Alantum 450µm Foam sample at Darcy superficial fluid flow velocity of $1.0x10^{-3} m.s^{-1}$ (R_{ED} = 0.0298).

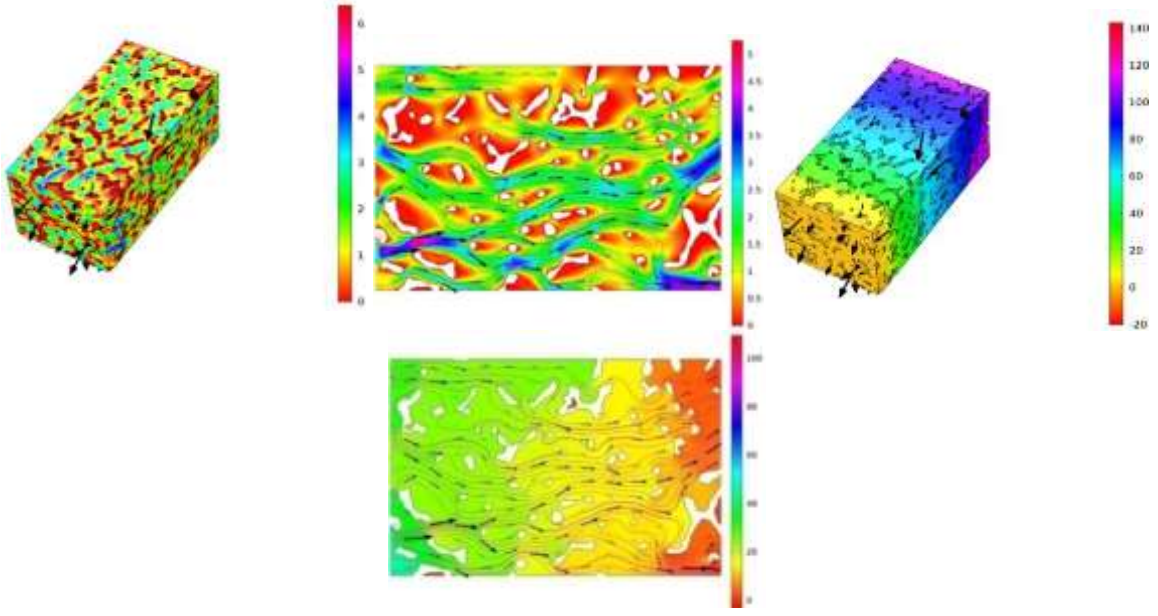

Appendix A_2: 3D and 2D Velocity ($m.s^{-1}$) and pressure (Pa) streamline plots of fluid flow across Alantum 450 µm Foam sample at Laminar superficial fluid flow velocity of $1.0m.s^{-1}$ (R_{ED} = 29.778).

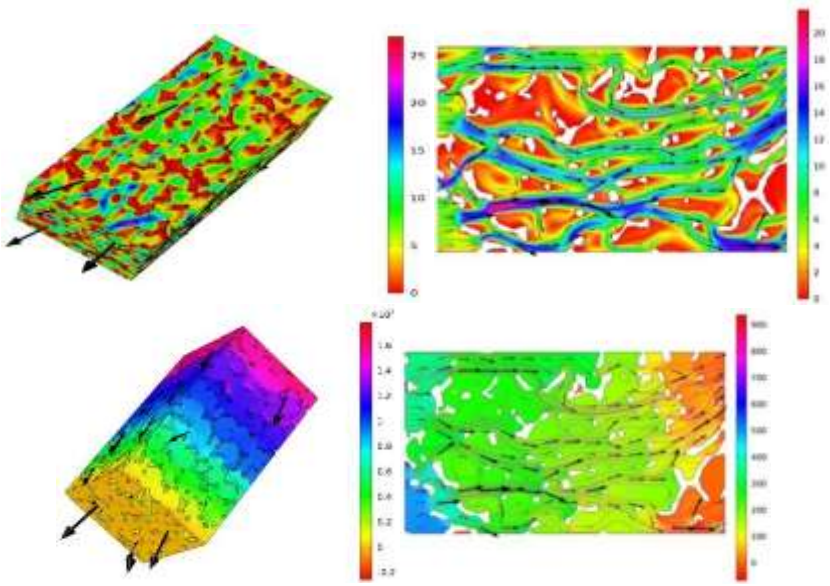

Appendix A_3 : 3D and 2D Velocity ($m.s^{-1}$) and pressure (Pa) streamline plots of fluid flow across Alantum 450µm Foam sample at Post-Laminar superficial fluid flow velocity of $5.985m.s^{-1}$ (R_{ED} = 148.9).

Appendix B: Velocity and Pressure Streamline Plots of Flow across Inconel (Alantum 1200µm)

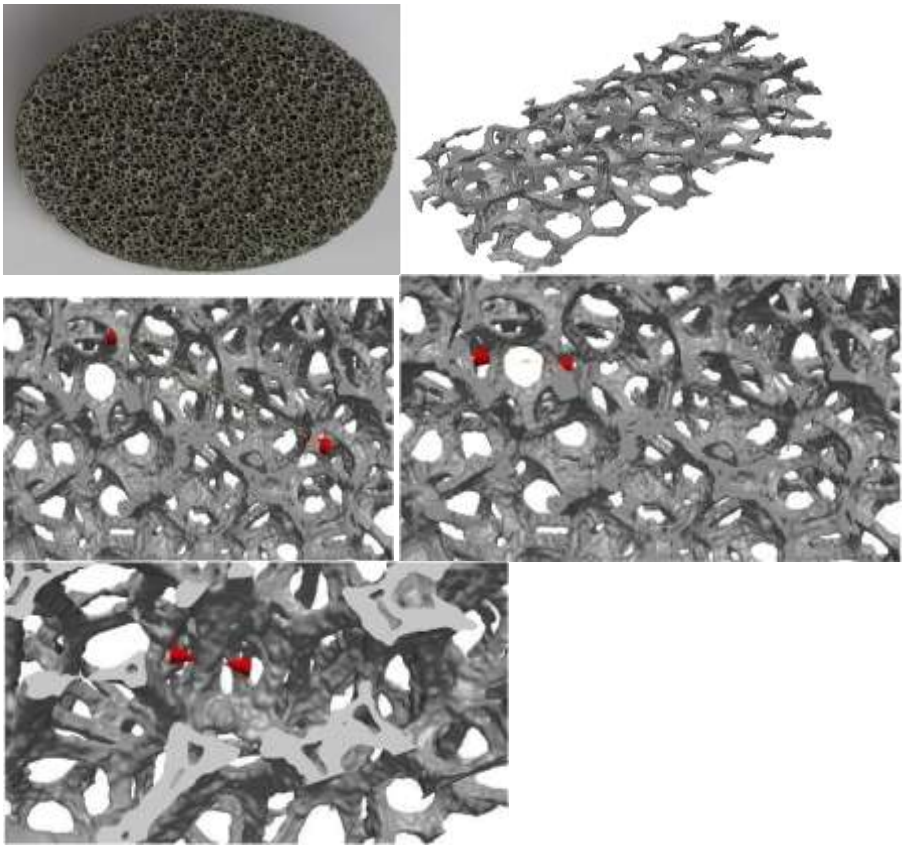

Appendix B1: Images of the internal morphology of Alantum 1200µm metal foam.

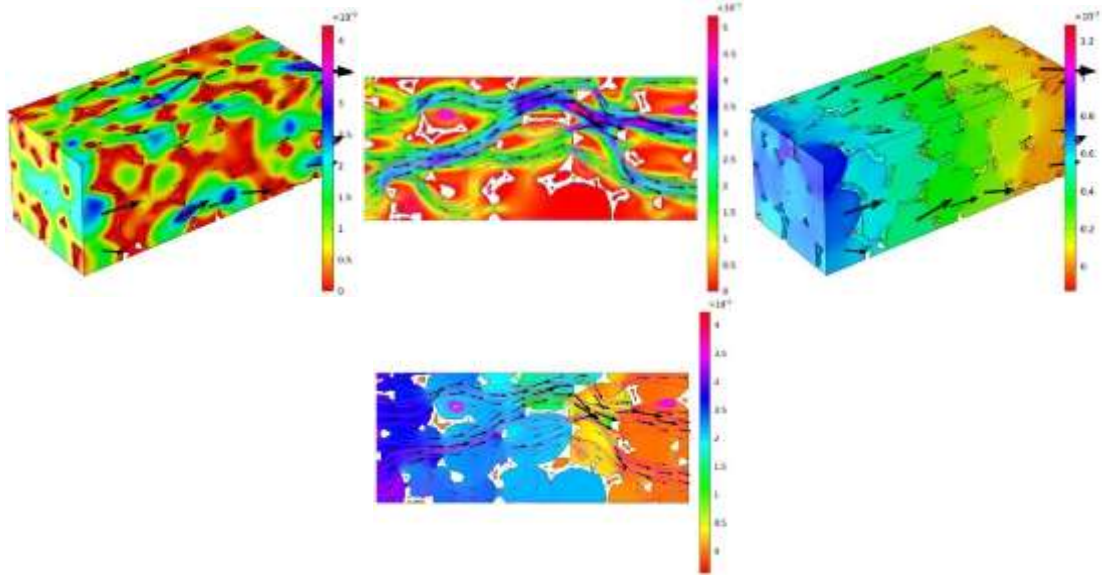

Appendix B2:3D and 2D Velocity ($m.s^{-1}$) and pressure (Pa) streamline plots of fluid flow across Alantum 1200 µm Foam sample at Darcy superficial fluid flow velocity of $1.0x10^{-3}m.s^{-1}$ (R_{ED} = 0.0814).

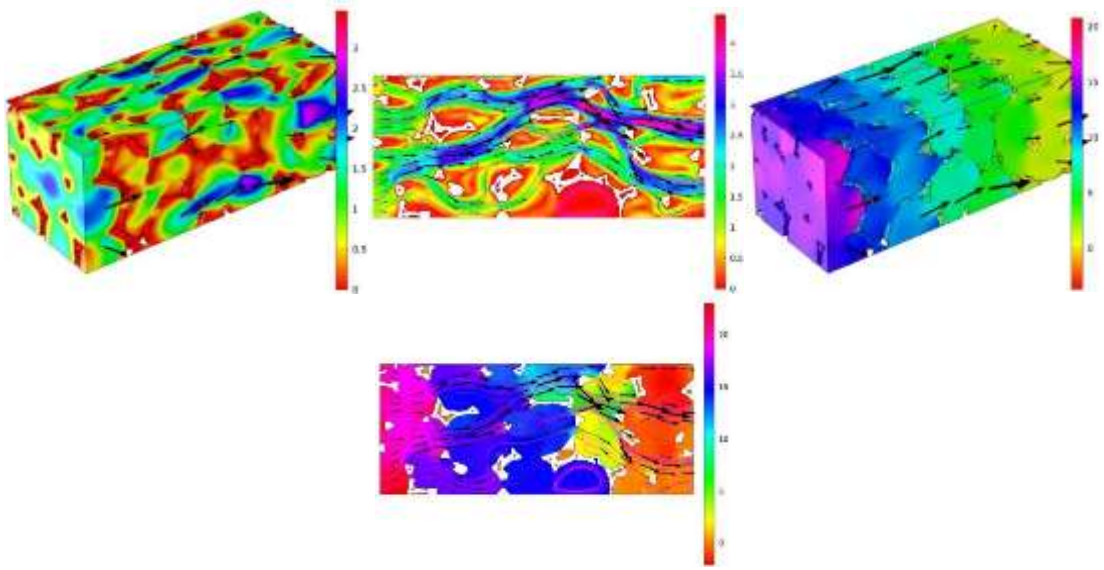

Appendix B$_3$: 3D and 2D Velocity (m.s^{-1}) and pressure (Pa) streamline plots of fluid flow across Alantum 1200µm Foam sample at Laminar superficial fluid flow velocity of 1.0m.s^{-1} (R_{ED} = 81.394).

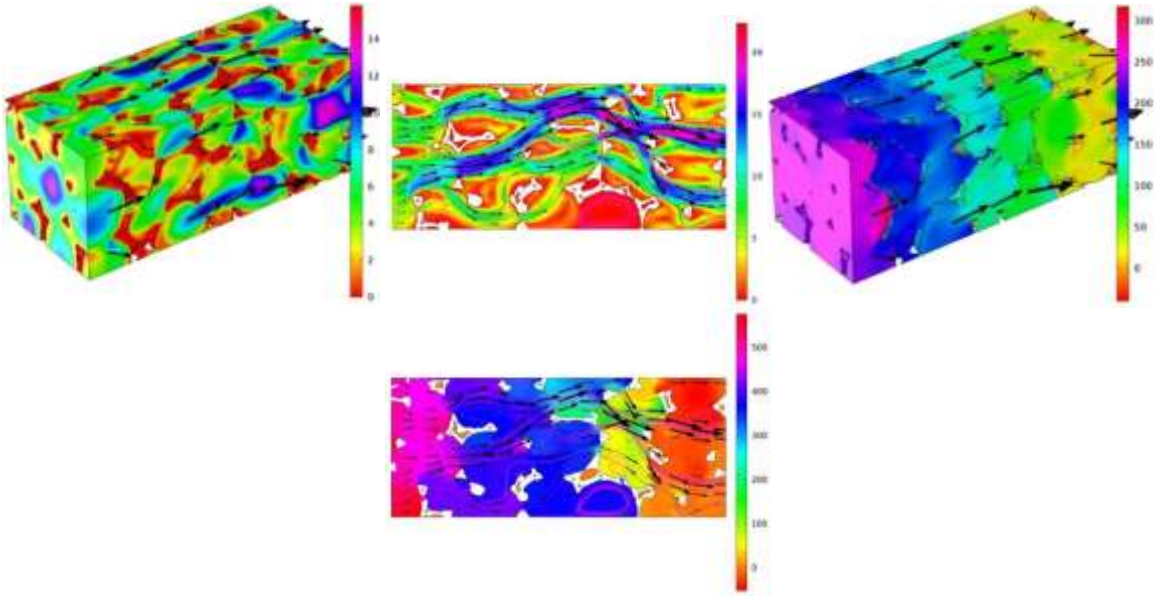

Appendix B$_4$: 3D and 2D Velocity (m.s^{-1}) and pressure (Pa) streamline plots of fluid flow across Alantum 1200µm Foam sample at Turbulence superficial fluid flow velocity of 5.0 m.s^{-1} (R_{ED} = 407).

Appendix C: Velocity and Pressure Streamline Plots of Flow across Recemat RCM-NCX 1723

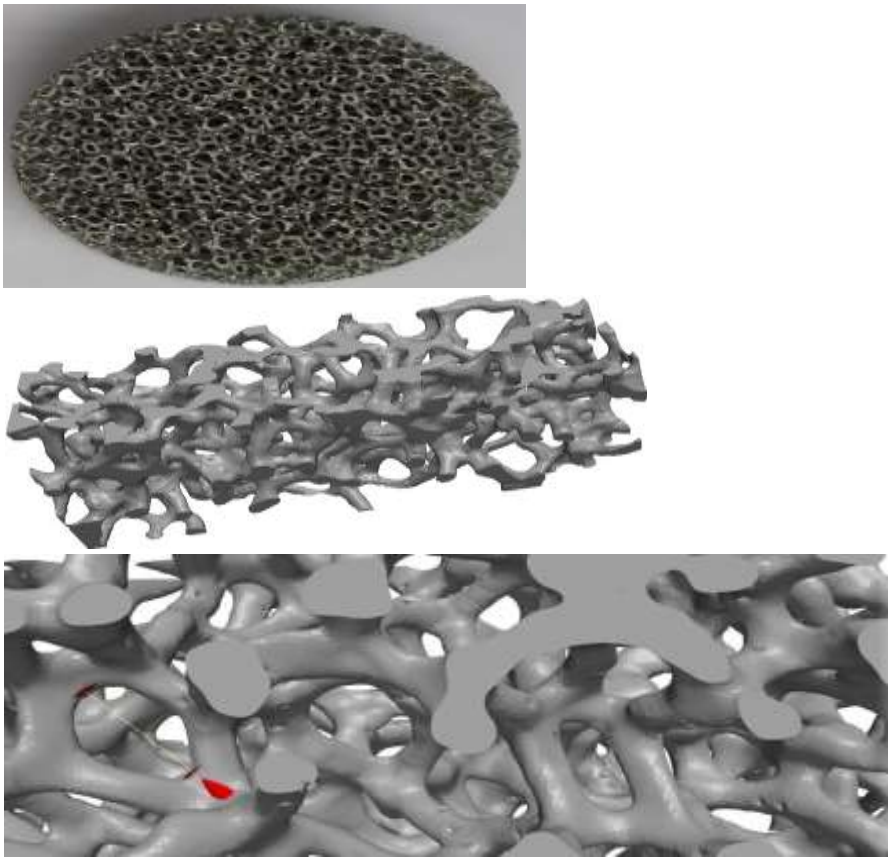

Appendix C_1: Images of the internal morphology of RCM-NCX 1723 metal foam.

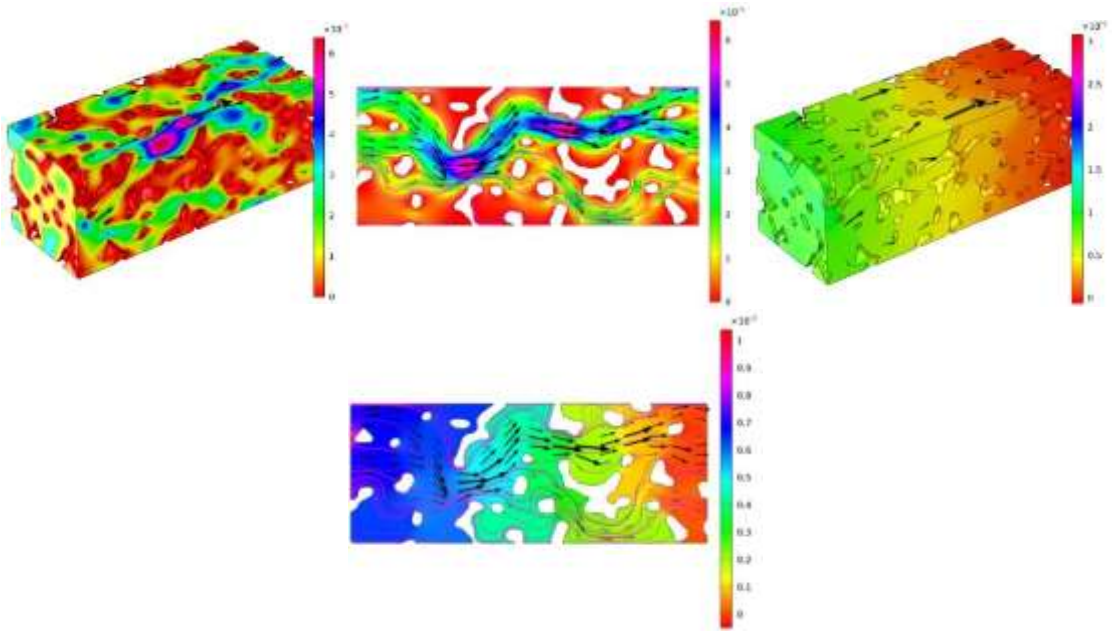

Appendix C$_2$: 3D and 2D Velocity (m.s^{-1}) and pressure (Pa) streamline plots of fluid flow across RCM-NCX 1723 Foam sample at Darcy superficial fluid flow velocity of 1.0x10^{-3}m.s^{-1} (R_{ED} = 0.123).

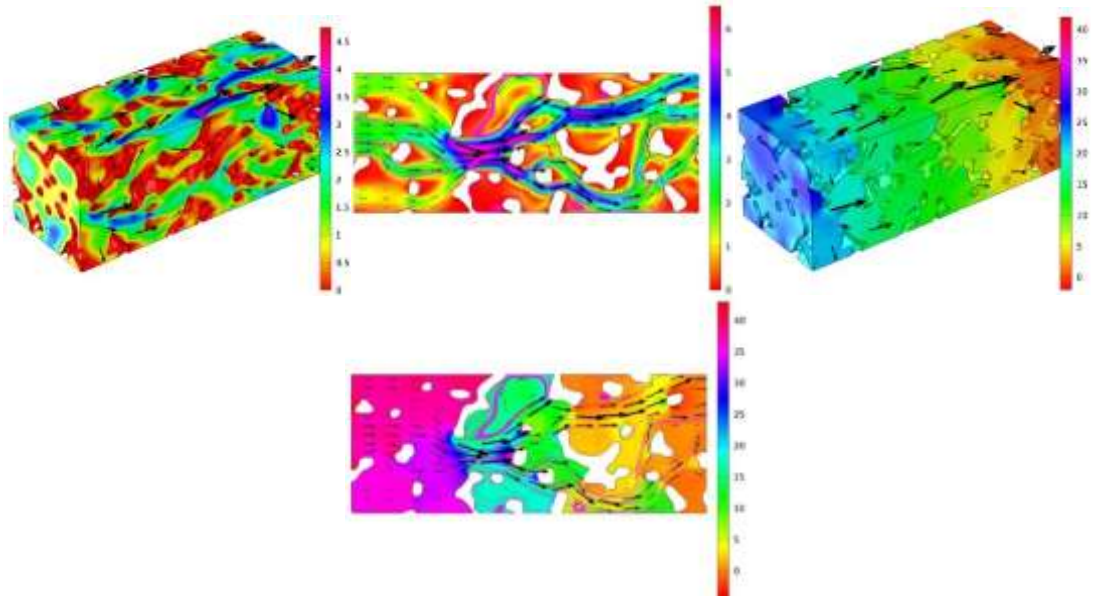

Appendix C$_3$: 3D and 2D Velocity (m.s^{-1}) and pressure (Pa) streamline plots of fluid flow across RCM-NCX Foam sample at Laminar superficial fluid flow velocity of 1.0m.s^{-1} (R_{ED} = 122.753).

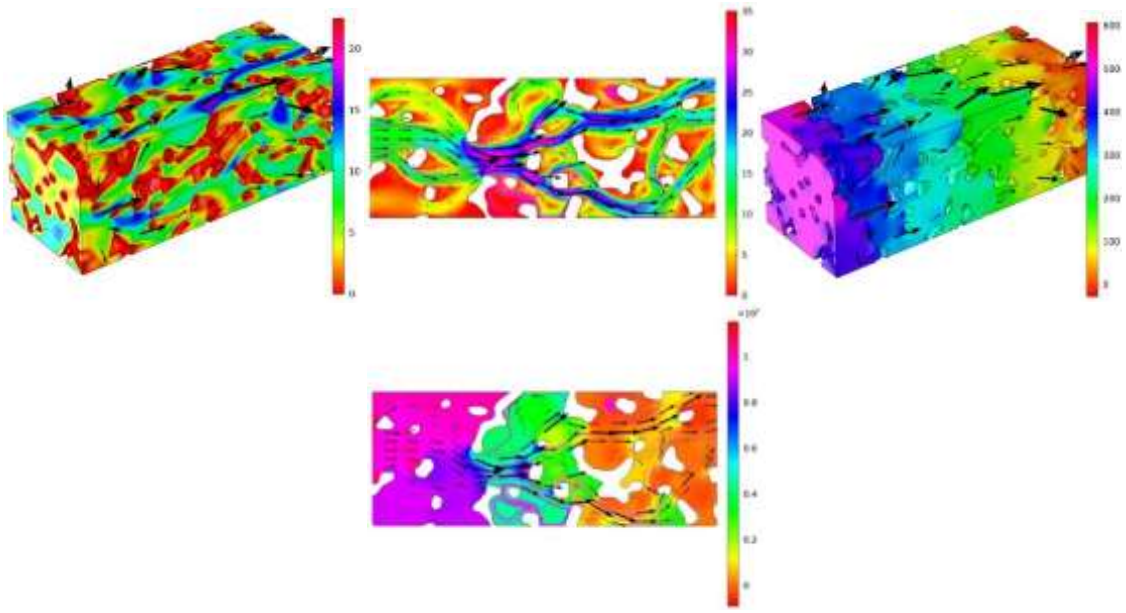

Appendix C$_4$: 3D and 2D Velocity (m.s^{-1}) and pressure (Pa) streamline plots of fluid flow across RCM-NCX Foam sample at Turbulence superficial fluid flow velocity of 5.0m.s^{-1} (R_{ED} = 407).

Appendix D: Velocity and Pressure Streamline Plots of Flow across Recemat RCM-NCX 1116

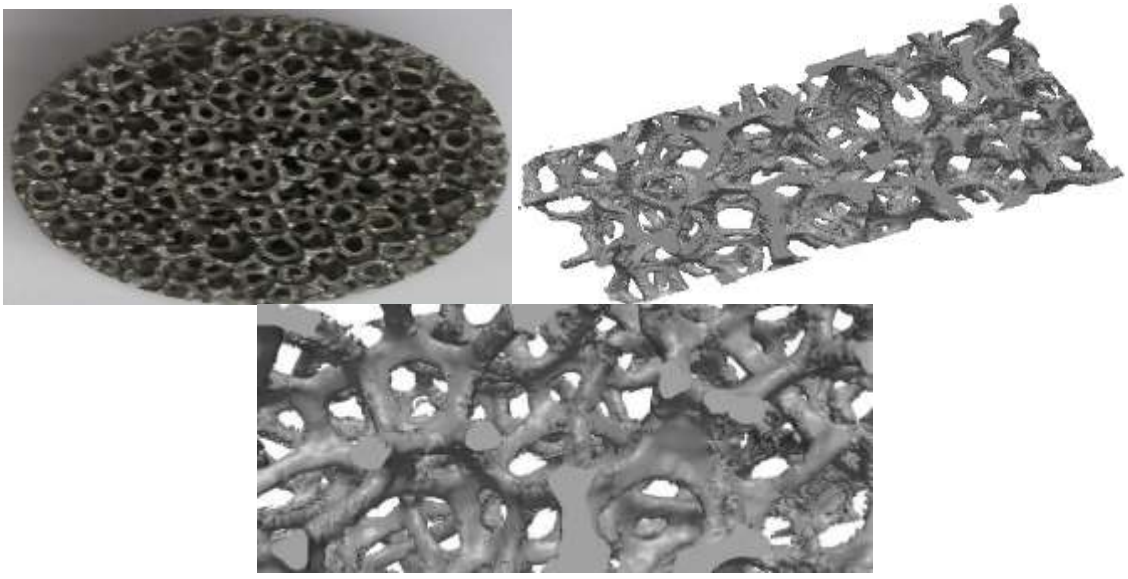

Appendix D1: Images of the internal morphology of RCM-NCX 1116 metal foam.

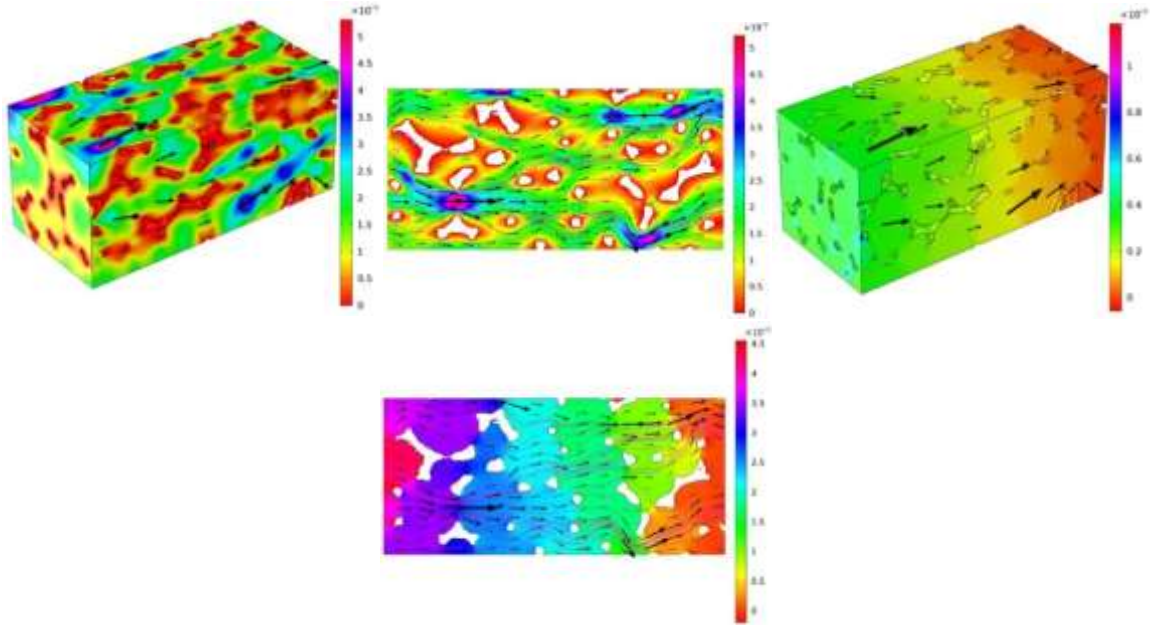

Appendix D2: 3D and 2D Velocity ($m.s^{-1}$) and pressure (Pa) streamline plots of fluid flow across RCM-NCX 1116 Foam sample at Darcy superficial fluid flow velocity of $1.0x10^{-3}m.s^{-1}$ (R_{ED} = 0.162).

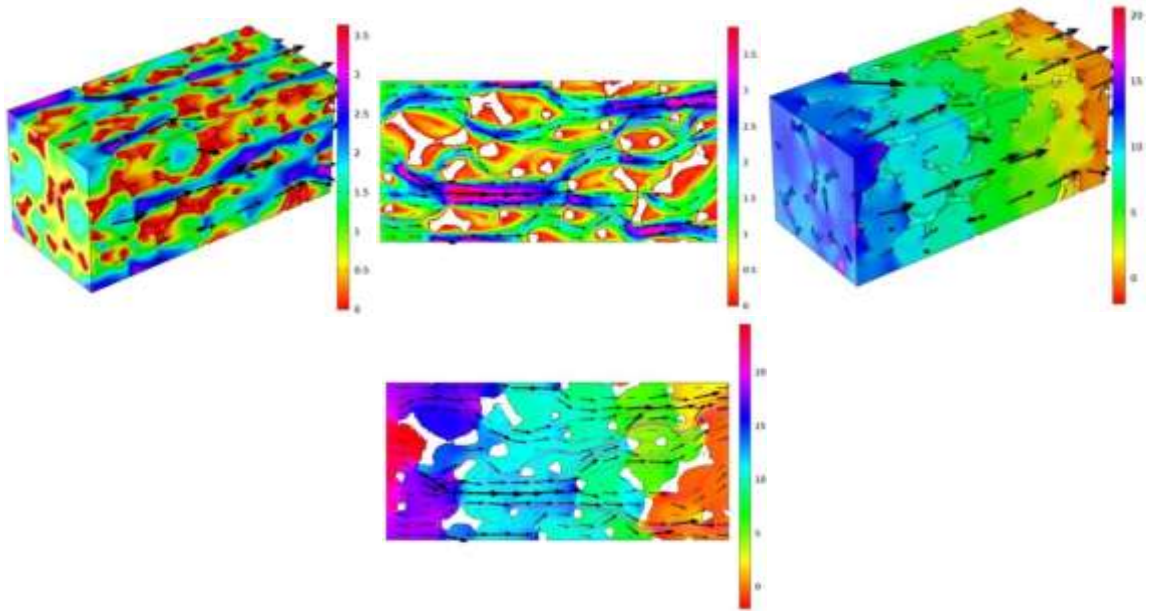

Appendix D3: 3D and 2D Velocity ($m.s^{-1}$) and pressure (Pa) streamline plots of fluid flow across RCM-NCX 1116 Foam sample at Laminar superficial fluid flow velocity of $1.0m.s^{-1}$ (R_{ED} = 162).

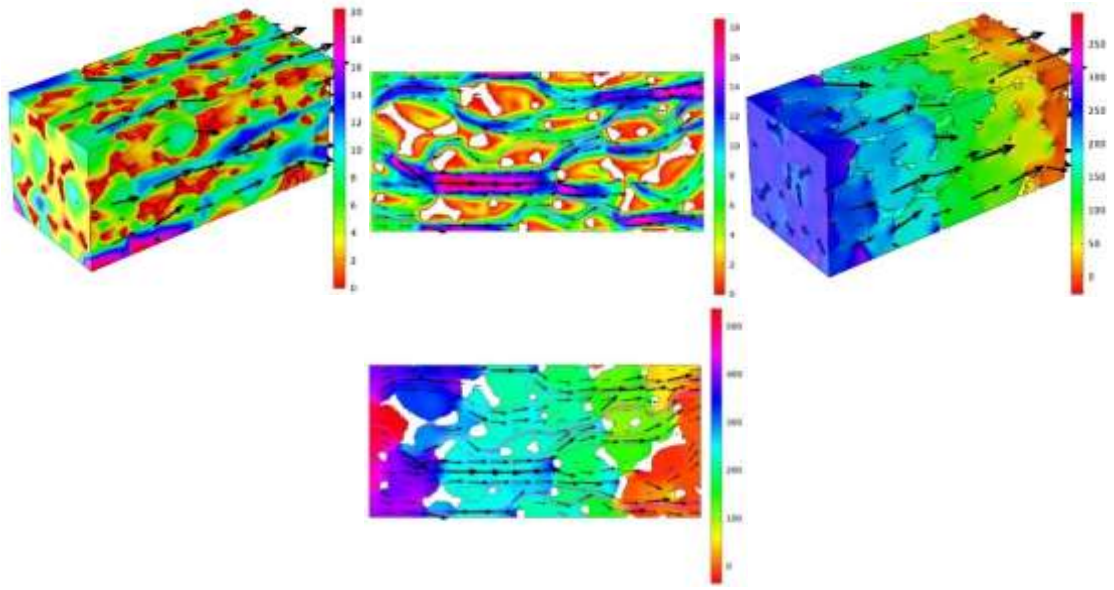

Appendix D$_4$: 3D and 2D Velocity (m.s^{-1}) and pressure (Pa) streamline plots of fluid flow across RCM-NCX 1116 Foam sample at Turbulence superficial fluid flow velocity of 5.0m.s^{-1} (R_{ED} = 812).

Appendix E: Velocity and Pressure Streamline Plots of Flow across Porvair 7PPI

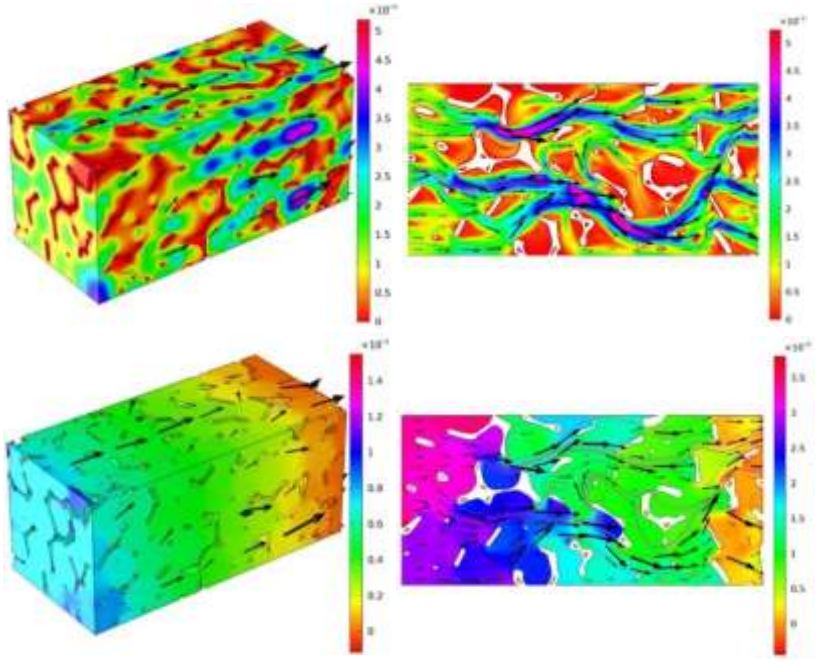

Appendix E$_1$: 3D and 2D Velocity (m.s^{-1}) and pressure (Pa) streamline plots of fluid flow across Porvair 7PPI Foam sample at Darcy superficial fluid flow velocity of 1.0x10^{-3}m.s^{-1} (R_{ED} = 0.097).

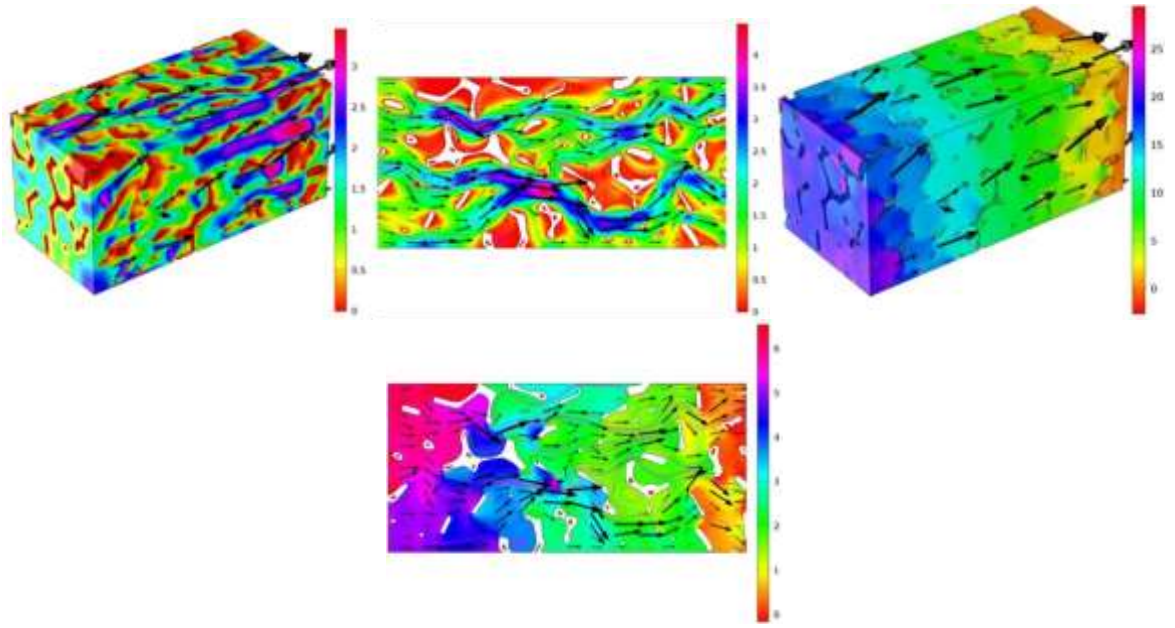

Appendix E$_2$: 3D and 2D Velocity (m.s^{-1}) and pressure (Pa) streamline plots of fluid flow across Porvair 7PPI Foam sample at Laminar superficial fluid flow velocity of 1.0m.s^{-1} (R_{ED} = 97).

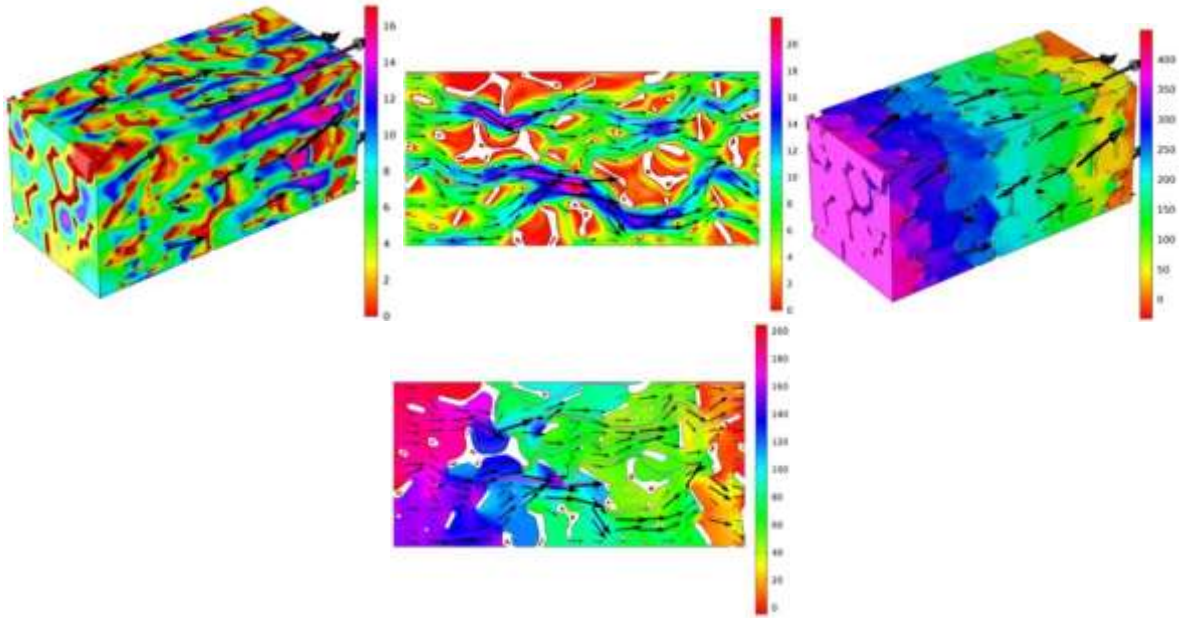

Appendix E_3: 3D and 2D Velocity ($m.s^{-1}$) and pressure (Pa) streamline plots of fluid flow across Porvair Foam sample at Turbulence superficial fluid flow velocity of $5.0m.s^{-1}$ (R_{ED} = 485).

Appendix F: Effects of Porous Metal Stacking and Entrance and Exit Effects on the Pressure Drop

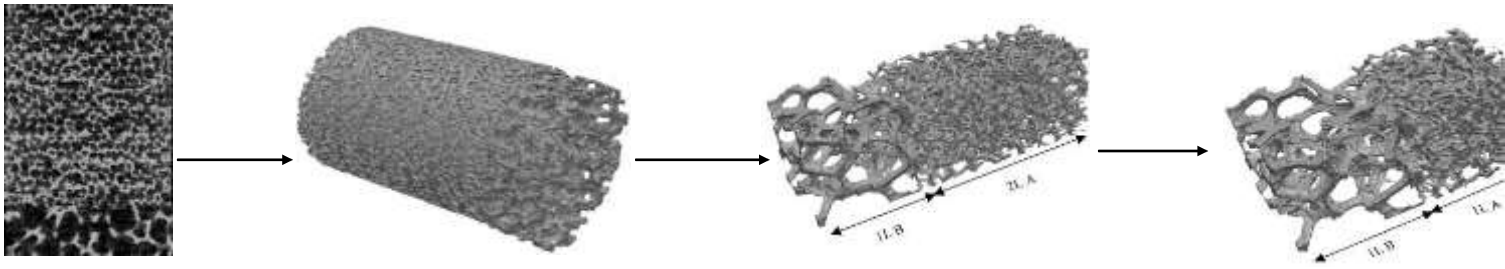

Appendix F_1: Images of the internal morphology of stacked Inc 450µm and Inc 1200µm porous metallic structures.

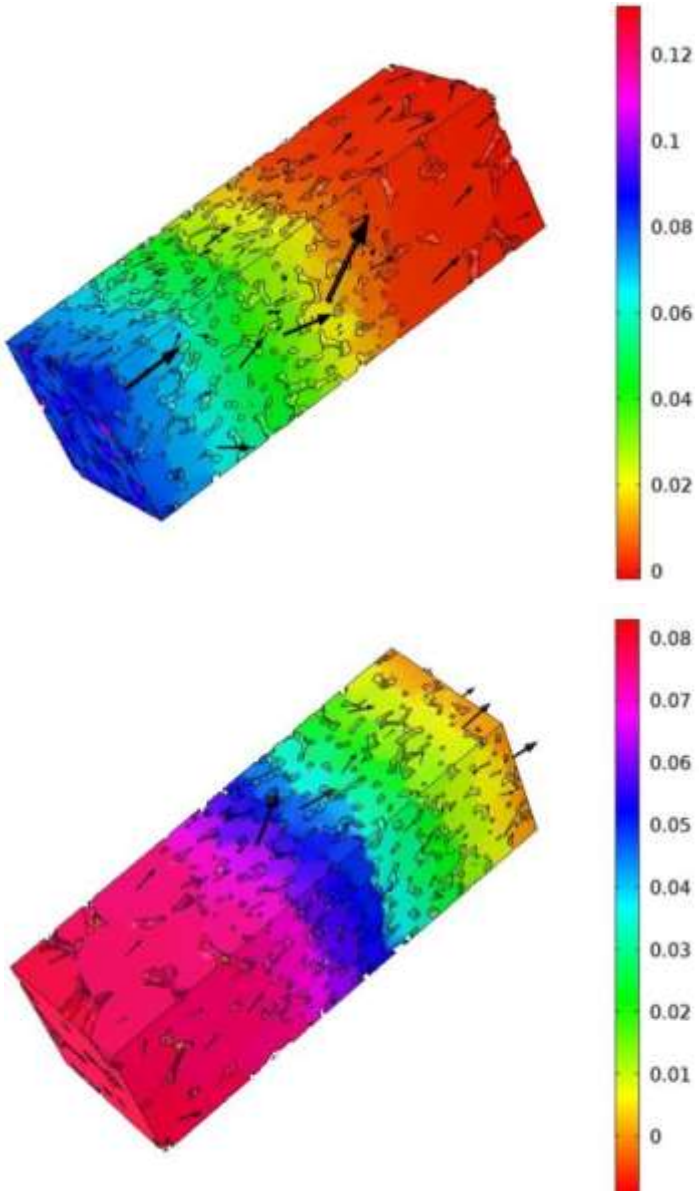

Appendix F2: Three-dimensional pressure profile plots for stacked porous samples(Inc 450µm and Inc 1200µm) at 10^{-3}m.s^{-1} superficial air inlet velocity indicating the presence of fluid at the inlet of (left) Inc 450µm and (right) 1200 µm samples (Sudden enlargement).

Appendix G: These will present from table (G_1 – G_9) the results of velocity, Re, superficial velocity, pressure drop and pressure drop per unit length of real, sudden enlargement and

sudden contraction of stacked samples obtained from CFD modeling and simulation of current work.

Table G_1: Alantum 450um Real

V (m/s)	Rep	Vp (m/s)	Pressure (Pa)	Pa/L
1.00E-06	2.978E-05	1.197E-06	7.38E-05	0.015
1.00E-04	2.978E-03	1.197E-04	7.38E-03	1.454
1.00E-03	2.978E-02	1.197E-03	0.073818	14.543
1.00E-02	0.2978	1.197E-02	0.73877	145.542
0.020	0.596	2.39E-02	1.4768	290.938
0.030	0.893	3.59E-02	2.2214	437.628
0.040	1.191	4.79E-02	2.9688	584.870
0.050	1.489	5.99E-02	3.7197	732.801
0.075	2.233	8.98E-02	5.6085	1104.905
0.100	2.9778	0.1197	7.5284	1483.136
0.500	14.8892	0.5985	44.9	8845.548
1.000	29.7784	1.1970	112.48	22159.180
1.232	36.6834	1.4746	152.2	29984.240
1.516	45.1488	1.8148	208.37	41050.039
1.800	53.6142	2.1551	272.98	53778.566
2.085	62.0796	2.4954	346.19	68201.340
2.3690	70.5450	2.8357	428.09	84336.091
3.0797	91.7085	3.6864	671.11	132212.372
3.7904	112.8720	4.5371	968.38	190776.202
4.5011	134.0355	5.3878	1318.8	259810.875
5.0000	148.8918	5.9850	1595.8	314381.403
6.0000	178.6701	7.1820	2226.3	438593.381

Table G2: Alantum 1200um Real

V (m/s)	Rep	Vp (m/s)	Pressure (Pa)	Pa/L
1.00E-06	8.139E-05	1.103E-06	7.19E-06	1.170E-03
1.00E-05	8.139E-04	1.103E-05	7.19E-05	1.170E-02
1.00E-04	8.139E-03	1.103E-04	7.19E-04	0.117
1.00E-03	8.139E-02	1.103E-03	0.0071882	1.170
1.00E-02	0.814	1.103E-02	0.071986	11.716
0.020	1.628	0.02207	0.14442	23.506
0.030	2.442	0.03310	0.21741	35.386
0.040	3.256	0.04414	0.29127	47.407
0.050	4.070	0.05517	0.36605	59.578
0.075	6.105	0.08276	0.55828	90.866
0.100	8.139	0.1103	0.75863	123.475
0.500	40.697	0.5517	5.3072	863.802
1.000	81.394	1.1035	14.522	2363.607
1.232	100.268	1.3594	20.144	3278.646
1.516	123.407	1.6731	28.237	4595.866
1.800	146.545	1.9868	37.685	6133.626
2.085	169.684	2.3005	48.521	7897.298
2.3690	192.823	2.6142	60.771	9891.113
3.0797	250.670	3.3984	97.713	15903.809
3.7904	308.517	4.1827	143.83	23409.831
4.5011	366.364	4.9670	199.18	32418.620
5.0000	406.971	5.517	243.49	39630.534
6.0000	488.365	6.621	346	56315.104

Table G3: RCM-NCX 1723 Real

V (m/s)	Rep	Vp (m/s)	Pressure (Pa)	Pa/L
1.00E-06	1.228E-04	1.235E-06	9.72E-06	0.001
1.00E-05	1.228E-03	1.235E-05	9.72E-05	0.011
1.00E-04	1.228E-02	1.235E-04	9.72E-04	0.108
1.00E-03	0.123	1.235E-03	0.0097219	1.076
1.00E-02	1.228	1.235E-02	0.097538	10.796
0.020	2.455	2.470E-02	0.1962	21.716
0.030	3.683	3.705E-02	0.29652	32.819
0.040	4.910	4.941E-02	0.39896	44.157
0.050	6.138	6.176E-02	0.50361	55.740
0.075	9.206	9.264E-02	0.77659	85.954
0.100	12.275	0.124	1.0717	118.616
0.500	61.377	0.618	8.324	921.306
1.000	122.753	1.235	24.774	2742.003
1.232	151.217	1.522	35.455	3924.184
1.516	186.113	1.873	51.225	5669.618
1.800	221.010	2.224	69.983	7745.766
2.085	255.906	2.575	91.709	10150.415
2.3690	290.802	2.926	116.37	12879.911
3.0797	378.043	3.804	190.71	21107.914
3.7904	465.283	4.682	282.89	31310.459
4.5011	552.524	5.560	392.66	43459.878
5.0000	613.765	6.176	480.06	53133.370
6.0000	736.518	7.411	680.76	75346.984

Table G4: RCM-NCX 1116 Real

V (m/s)	Rep	Vp (m/s)	Pressure (Pa)	Pa/L
1.00E-06	1.624E-04	1.113E-06	3.775E-06	2.785E-04
1.00E-05	1.624E-03	1.113E-05	3.775E-05	2.785E-03
1.00E-04	1.624E-02	1.113E-04	3.775E-04	2.785E-02
1.00E-03	0.162	1.113E-03	3.775E-03	0.2785
1.00E-02	1.624	1.113E-02	3.790E-02	2.796
0.020	3.248	2.227E-02	7.647E-02	5.642
0.030	4.872	0.033404225	0.116	8.564
0.040	6.496	0.044538966	0.157	11.586
0.050	8.120	0.055673708	0.199	14.716
0.075	12.179	0.083510561	0.313	23.071
0.100	16.239	0.111347415	0.437	32.205
0.500	81.196	0.556737075	3.892	287.155
1.000	162.391	1.113474151	12.326	909.399
1.232	200.047	1.371667462	17.882	1319.315
1.516	246.211	1.688206107	26.154	1929.615
1.800	292.376	2.004744752	36.043	2659.215
2.085	338.541	2.321283397	47.550	3508.189
2.3690	384.705	2.637822042	60.657	4475.210
3.0797	500.117	3.429168655	100.370	7405.194
3.7904	615.528	4.220515268	149.880	11057.990
4.5011	730.940	5.01186188	209.060	15424.229
5.0000	811.957	5.567	256.32	18911.023
6.0000	974.348	6.681	365.12	26938.173

Table G5: Porvair Real 7PPI

V (m/s)	Rep	Vp (m/s)	Pressure (Pa)	Pa/L
1.00E-06	9.701E-05	1.1150E-06	7.55E-06	7.223E-04
1.00E-05	9.701E-04	1.1150E-05	7.55E-05	7.223E-03
1.00E-04	9.701E-03	1.1150E-04	7.55E-04	7.223E-02
1.00E-03	9.701E-02	1.1150E-03	0.0075533	7.224E-01
1.00E-02	0.970	1.1150E-02	0.075711	7.241E+00
0.020	1.940	2.2299E-02	0.15209	14.546
0.030	2.910	0.0334	0.2292	21.920
0.040	3.880	0.0446	0.30842	29.497
0.050	4.851	0.0557	0.3886	37.165
0.075	7.276	0.0836	0.59873	57.262
0.100	9.701	0.1115	0.8226	78.673
0.500	48.506	0.5575	6.4729	619.061
1.000	97.011	1.1150	19.149	1831.389
1.232	119.506	1.3735	27.236	2604.820
1.516	147.085	1.6904	39.141	3743.401
1.800	174.663	2.0074	53.301	5097.647
2.085	202.241	2.3244	69.754	6671.194
2.3690	229.820	2.6413	88.515	8465.474
3.0797	298.766	3.4337	145.57	13922.150
3.7904	367.712	4.2261	216.99	20752.678
4.5011	436.658	5.0185	302.56	28936.496
5.0000	485.056	5.5748	370.98	35480.107
6.0000	582.068	6.6897	528.69	50563.313

Table G6: Inc 450+1200μm (5.004+2.556mm) 2LA+1LB (Sudden enlargement)

V (m/s)	Vp (m/s)	Pressure (Pa)	Pa/L
1.00E-06	1.185E-06	8.431E-05	0.011
1.00E-05	1.185E-05	8.431E-04	0.112
1.00E-04	1.185E-04	0.00843	1.115
1.00E-03	1.185E-03	0.084	11.153
1.00E-02	1.185E-02	0.844	111.623
0.020	2.370E-02	1.690	223.519
0.030	3.555E-02	2.538	335.767
0.040	4.740E-02	3.391	448.479
0.050	5.926E-02	4.248	561.839
0.075	8.888E-02	6.410	847.870
0.100	0.1185	8.610	1138.942
0.500	0.5926	51.874	6861.640
1.000	1.1851	131.16	17349.206
1.232	1.4599	178.06	23552.910
1.516	1.7968	244.62	32357.143
1.800	2.1337	321.41	42514.550
2.085	2.4706	408.57	54043.651
2.3690	2.8075	506.23	66961.640
3.0797	3.6498	796.38	105341.270
3.7904	4.4920	1151.6	152328.042
4.5011	5.3343	1570.6	207751.323
5.0000	5.9255	1902.0	251587.302
6.0000	7.1106	2660.144	351870.899

Table G7: Inc 1200+450μm (2.556+5.004mm) 1LB+2LA (Sudden contraction)

V (m/s)	Vp (m/s)	Pressure (Pa)	Pa/L
1.00E-06	1.185E-06	7.853E-05	0.010
1.00E-05	1.185E-05	7.853E-04	0.104
1.00E-04	1.185E-04	7.853E-03	1.039
1.00E-03	1.185E-03	0.079	10.389
1.00E-02	1.185E-02	0.786	103.991
0.020	2.370E-02	1.575	208.267
0.030	3.555E-02	2.366	312.923
0.040	4.740E-02	3.160	418.042
0.050	5.926E-02	3.956	523.254
0.075	8.888E-02	5.978	790.794
0.100	0.1185	8.034	1062.698
0.500	0.593	48.667	6437.434
1.000	1.185	123.180	16293.651
1.232	1.460	167.320	22132.275
1.516	1.797	229.94	30415.344
1.800	2.134	302.160	39968.254
2.085	2.471	384.160	50814.815
2.3690	2.808	476.050	62969.577
3.0797	3.650	749.050	99080.688
3.7904	4.492	1083.600	143333.333
4.5011	5.334	1478.400	195555.556
5.0000	5.926	1791.400	236957.672
6.0000	7.111	2503.600	331164.021

Table G8: Inc 450+1200μm (2.504+2.556mm) 1LA+1LB (Sudden enlargement)

V (m/s)	Vp (m/s)	Pressure (Pa)	Pa/L
1.00E-06	1.172E-06	4.727E-05	0.009
1.00E-05	1.172E-05	4.727E-04	0.093
1.00E-04	1.172E-04	4.727E-03	0.934
1.00E-03	1.172E-03	4.727E-02	9.342
1.00E-02	1.172E-02	0.473	93.504
0.020	2.343E-02	0.947	187.150
0.030	3.515E-02	1.423	281.186
0.040	4.687E-02	1.900	375.573
0.050	5.858E-02	2.380	470.336
0.075	8.787E-02	3.591	709.723
0.100	0.1172	4.825	953.458
0.500	0.5858	28.833	5698.221
1.000	1.1717	72.570	14341.897
1.232	1.4433	98.353	19437.352
1.516	1.7764	134.980	26675.889
1.800	2.1095	177.210	35021.739
2.085	2.4426	225.100	44486.166
2.3690	2.7757	278.700	55079.051
3.0797	3.6084	437.600	86482.213
3.7904	4.4411	631.570	124816.206
4.5011	5.2738	859.730	169907.115
5.0000	5.8583	1039.800	205494.071
6.0000	7.0300	1449.100	286383.399

Table G9: Inc 1200+450μm (2.556+2.504mm) 1LB+1LA (Sudden contraction)

V (m/s)	Vp (m/s)	Pressure (Pa)	Pa/L
1.00E-06	1.172E-06	4.393E-05	0.00868
1.00E-05	1.172E-05	4.393E-04	0.08681
1.00E-04	1.172E-04	4.393E-03	0.86812
1.00E-03	1.172E-03	4.394E-02	8.683
1.00E-02	1.172E-02	0.440	86.990
0.020	2.343E-02	0.882	174.324
0.030	3.515E-02	1.327	262.233
0.040	4.687E-02	1.775	350.711
0.050	5.858E-02	2.225	439.743
0.075	8.787E-02	3.368	665.652
0.100	0.117	4.539	897.036
0.500	0.586	28.091	5551.581
1.000	1.172	72.097	14248.419
1.232	1.443	98.260	19418.972
1.516	1.776	135.640	26806.324
1.800	2.110	228.340	45126.482
2.085	2.443	228.340	45126.482
2.3690	2.776	283.670	56061.265
3.0797	3.608	448.340	88604.743
3.7904	4.441	650.520	128561.265
4.5011	5.274	889.100	175711.462
5.0000	5.858	1077.600	212964.427
6.0000	7.030	1507.400	297905.138

Meshing

2D LTM Mesh Number of Degree of Freedom solved 64900

2D LTM Optimised 1.4111Pa

2D Extremely fine mesh 1.409Pa

Extremely fine 2D triangular mesh structure consisting of 179980 domain elements and 5214 boundary elements

Image resolution = 0.012

Curvature factor = 0.25

Resolution in the narrow region = 1

Growth rate = 1.3

3D LTM Optimised Mesh Density = 3805084

3D LTM Mesh k_0/m^2 = 1.25e-09m^2

Fluid Viscosity = 1.82 x 10^{-5}Pa.s

Fluid Density = 1.2047kg/m^3

Inconel™ 450µm length; x = 2.508mm, y = 2.508mm & z = 5.076mm

Inconel™ 1200µm length; x = 2.556mm, y = 2.556mm & z = 2.144mm

Recemat™ 1116 PPI length; x = 6.2377mm, y = 6.2377mm & z = 13.554mm

Recemat™ 1723 PPI length; x = 3.542mm, y = 3.542mm & z = 9.035mm

Povair 7 PPI length; x = 4.9206mm, y = 4.9026mm & z = 12.126mm